ISSN: 3023 - 8544

ADBA

# COMPUTER SCIENCE

VOLUME 2, ISSUE 2, JULY 2025

AN INTERDISCIPLINARY JOURNAL OF
COMPUTER SCIENCE

https://journals.**adbascientific**.com/acs

ISSN: 3023-8544

ADBA Computer Science
Volume: 2 – Issue No: 2 (July 2025)

# EDITORIAL BOARD

## Editor-in-Chief

Dr. Fatih Kurugollu, University of Sharjah, UAE, fkurugollu@sharjah.ac.ae

## Associate Editors

Dr. Chunbiao Li, Nanjing University of Information Science and Technology, CHINA, chunbiaolee@nuist.edu.cn
Dr. René Lozı, University Cote d'Azur, FRANCE, rene.lozi@univ-cotedazur.fr
Dr. Yeliz Karaca, University of Massachusetts Chan Medical School, USA, yeliz.karaca@ieee.org

## Editorial Board Members

Dr. J. M. Munoz-Pacheco, Benemérita Universidad Autónoma de Puebla, MEXICO, jesusm.pacheco@correo.buap.mx
Dr. Mehmet Yavuz, Kyrgyz-Turkish Manas University, KYRGYZSTAN, mehmet.yavuz@manas.edu.kg
Dr. Salah Mahmoud Boulaaras, Qassim University, SAUDI ARABIA, s.boularas@qu.edu.sa
Dr. Christos K. Volos, Aristotle University of Thessaloniki, GREECE, volos@physics.auth.gr
Dr. Karthiekeyan Rajagopal, SRM Group of Institutions, INDIA, rkarthiekeyan@gmail.com
Dr. Unal Cavusoglu, Sakarya University, TURKIYE, unalc@sakarya.edu.tr
Dr. Zhouchao Wei, China University of Geosciences, CHINA, weizhouchao@163.com
Dr. Ali Akgül, Siirt University, TURKIYE, aliakgul@siirt.edu.tr
Dr. Viet-Thanh Pham, Industrial University of Ho Chi Minh City, VIETNAM, thanh.phamviet@hust.edu.vn
Dr. Jorge E. Macías-Díaz, Universidad Autónoma de Aguascalientes, MEXICO, jemacias@correo.uaa.mx
Dr. Iqtadar Hussain, Qatar University, QATAR, iqtadarqau@qu.edu.qa
Dr. Bilel Selmi, Université de Monastir, TUNISIA, bilel.selmi@fsm.rnu.tn
Dr. Guillermo Huerta Cuellar, Universidad de Guadalajara, MEXICO, guillermo.huerta@academicos.udg.mx

## Editorial Advisory Board Members

Dr. Selman Hizal, Sakarya University of Applied Sciences, TURKIYE, selmanhizal@subu.edu.tr
Dr. Mehmet Zeki Konyar, Kocaeli University, TURKIYE, mzeki.konyar@kocaeli.edu.tr
Dr. Abdullah Gökyıldırım, Bandırma Onyedi Eylül University, TURKIYE, agokyildirim@bandirma.edu.tr

## Language Editor

Dr. Emir Avcıoğlu, Hitit University, TURKIYE, emiravcioglu@hitit.edu.tr

## Technical Coordinator

Dr. Burak Arıcıoğlu, Sakarya University of Applied Sciences, TURKIYE, baricioglu@subu.edu.tr

https://journals.adbascientific.com/acs/about/editorialTeam

ISSN: 3023-8544

ADBA Computer Science
Volume: 2 – Issue No: 2 (July 2025)

# CONTENTS

https://journals.adbascientific.com/acs/issue/view/15

**e-ISSN: 3023-8544**
**RESEARCH ARTICLE**
**Vol.**2 / **No.**2 / 2025 / **pp.**30-35
https://doi.org/10.69882/adba.cs.2025071

# Chaos Annihilation-Based on Genetic Algorithms in a Non-smooth Air-gap Permanent Magnet Synchronous Motor Embedded in the Microcontroller

**Isidore Komofor Ngongiah** [*,1], **Rolande Tsapla Fotsa** [β,2], **Joseph Mvogo Ngono** [α,3], **Noel Nyang Kibanya** [γ,4], **Emile Godwe** [δ,5] **and Foutse Momo** [σ,6]

[*] Department of Mechanical, Petroleum and Gas Engineering, National Advanced School of Mines and Petroleum Industries, University of Maroua, P.O. Box 46, Maroua, Cameroon, [β] Department of Mechanical Engineering, College of Technology, University of Buea, P.O. BOX 63 Buea, Cameroon, [α] Applied Computing Laboratory, Faculty of Science, University of Douala, P.O. Box 2701, Douala, Cameroon, [γ] Department of Physics, Faculty of Science, University of Bamenda, P.O. Box 39 Bamenda, Cameroon, [δ] Department of Physics, Faculty of Science, University of Maroua, P.O. Box 814, Cameroon, [σ] Biomedical Engineering, Energy and Modeling Laboratory (BEEMo.Lab.), Higher Institute of Science and Technology (HIST), University of Mountains, P.O. Box 208, Bangangte, Cameroon.

**ABSTRACT** This paper is devoted to the dynamical probing, microcontroller execution, and chaos annihilation based on genetic algorithms (GAs) in a non-smooth air-gap permanent magnet synchronous motor (NSAGPMSM) without external disturbances. The numerical simulations of NSAGPMSM in the absence of external disturbances reveal the existence of two different shapes of chaotic characteristics, reverse period doubling and periodic characteristics. The dynamical characteristics are certified by the microcontroller execution of NSAGPMSM in the absence of external disturbances. By optimizing the parameters of NSAGPMSM in the absence of external disturbances, thanks to the convergence of the objective function and its convergence rate, it is proven that GAs is effective in optimizing system parameters, leading to annihilation of chaos in the system to one of its three steady states.

**KEYWORDS**
Non-smooth air-gap
Permanent magnet synchronous motor
Microcontroller execution
Annihilation of chaos
Genetic algorithms

## INTRODUCTION

The introduction of high-performance permanent magnets, such as rare-earth magnets, has led to the development of a new generation of synchronous machines (Kiener *et al.* 1984; Pouillange 1987; Song *et al.* 2015). Due to their superior properties, such as high efficiency, compact size, high torque-to-weight ratio, high power density, fault tolerance, and low maintenance, permanent magnet synchronous motors are widely used in many industrial applications, such as machine tools, industrial robots, air conditioners, and packaging machines (Ananthamoorthy and Baskaran 2015; Chan and Chau 1997; Do *et al.* 2014a). However, these uses are not without challenges, particularly in the face of growing energy, industrial, and automotive concerns. Permanent magnet synchronous motors with non-smooth air gaps may exhibit instability during operation and may be subject to physical phenomena, such as chaos, which can lead to a complete collapse of the drive system (Machkour *et al.* 2022; Liao *et al.* 2017). These disturbances can be caused by mechanical vibrations (rotor imbalance), abrupt variations in the applied load, etc. To overcome these challenges, it is essential to develop innovative control strategies that take the performance of NSAGPMSM into account.

The high performance of permanent magnet synchronous motors depends on the absence of chaos (Iqbal and Singh 2019; Takougang Kingni *et al.* 2020; Tsapla Fotsa *et al.* 2025), without considering the impact of variations in the saliency ratio through the quadrature inductance. It should be noted that while variations in quadrature inductance are not always beneficial due to the potential for chaotic behavior, they can lead to an increase in the amplitude of angular velocity. However, it is important to note that in permanent magnet synchronous motors, the direct and

**Manuscript received:** 12 May 2025,
**Revised:** 16 July 2025,
**Accepted:** 16 July 2025.

[1] ngongiahisidore@gmail.com (**Corresponding author**)
[2] rtsapla@yahoo.com
[3] jmvogo@univ-douala.cm
[4] nyangnoelkibanya@gmail.com
[5] willgod7@yahoo.com
[6] mfoutse@yahoo.fr

quadrature inductances must be different (Yamdjeu *et al.* 2024, 2025).

To eliminate chaotic behaviors in permanent magnet synchronous motors, researchers have employed various control methods, such as control using Lyapunov's principle for global asymptotic stability (Kemnang Tsafack *et al.* 2020; Natiq *et al.* 2022; Do *et al.* 2014b), simple adaptive sliding mode control (Kemnang Tsafack *et al.* 2020; Maeng and Choi 2013), fuzzy adaptive control schemes (Luo 2014), passive control schemes (Wang *et al.* 2005), model predictive control, feedback control schemes (Du-Qu and Xiao-Shu 2008), dithering signal control schemes (Tung and Chen 1993; Wei and Wang 2013), and chaos control based on GAs to optimize the performance of NSAGPMSM with temperature through the objective function value (Yamdjeu *et al.* 2025; Cvetkovski and Petkovska 2016).The authors of (Yamdjeu *et al.* 2024) studied the dynamics, microcontroller implementation, and control approach in NSAGPMSM without external disturbances.

The NSAGPMSM without external disturbances displayed bistable chaos, periodic spikes, chaotic spikes, coexistence of periodic and chaotic characteristics, and a period-doubling route to monostable chaos. Two single controllers were used to bring chaos back to stable operation, with the second single controller being more effective due to its ability to meet selection criteria such as settling time and peak overshoot. Chaos annihilation based on GAs in NSAGPMSM without external disturbances embedded in the microcontroller is investigated in this paper.

The choice of the latter method is inspired by natural evolution, as GAs use techniques such as inheritance, mutation, selection, and crossover to generate solutions to optimization problems. Its versatility makes it a powerful tool for global optimization and the analysis of large data sets (Markku *et al.* 2007; Tian *et al.* 2019). Many researchers have focused on using GAs to reduce harmful vibrations or eliminate noise in permanent magnet synchronous motors (Pinto *et al.* 2024; Yi and Hsu 2003; Randi *et al.* 2013). This paper is organized into an introduction, two sections, and the conclusion: Section two presents the dynamical probing and microcontroller execution in NSAGPMSM without external disturbances. Section three brings out the chaos annihilation in NSAGPMSM without external disturbances based on GAs. The conclusion highlights a summary of the paper.

## DYNAMICAL PROBING AND MICROCONTROLLER EXECUTION IN NSAGPMSM WITHOUT EXTERNAL DISTURBANCES

The PMSM is presented in Fig. 1.

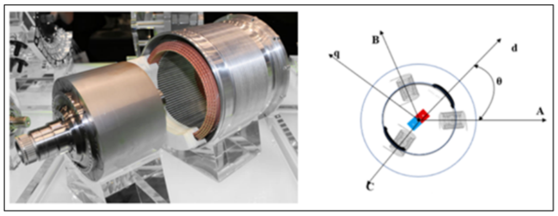

**Figure 1** Permanent Magnet Synchronous Motors (PMSM) and its space representation (Grellet and Clerc 1997; Caron and Hautier 1995).

The PMSM is presented in Fig. 1. Phase transformation is a key technique in designing and controlling PMSM, converting a three-axis reference frame to a two-axis frame to simplify the motor's differential equations (Grellet and Clerc 1997). The machine electrical equations in matrix form is given by (Caron and Hautier 1995):

$$[V_{Sabc}] = [R][I_{Sabc}] + \frac{d}{dt}[\psi_{Sabc}], \tag{1}$$

The stator voltage $V_{Sabc}$ is represented as a resistive term $R$ multiplied by the axes current components $I_{Sabc}$ and a flux variation term $\psi_{Sabc}$.

The magnetic equations defined by the stator flux equations can be expressed in matrix form as follows:

$$[\psi_{Sabc}] = [L][I_{Sabc}] + [\psi_{rabc}]. \tag{2}$$

The stator flux includes the self-flux and the flux generated by the magnets. The fluxes $\psi_{rabc}$ are the rotor fluxes as seen by the stator windings given by:

$$\psi_{rabc} = \psi_m \begin{pmatrix} \cos\theta \\ \cos(\theta - 2\pi/3) \\ \cos(\theta - 4\pi/3) \end{pmatrix}, \tag{3}$$

where $\psi_m$ is the constant magnet flux located along the direct axis of the (d-q) frame. The mechanical equation is given by:

$$C_{em} - C_r = J\frac{d\Omega_r}{d\tau} + f_v\Omega_r, \tag{4}$$

where $C_{em}$ is the electromagnetic torque, $C_r$ is the load torque, $\frac{d\Omega_r}{d\tau}$ is the angular acceleration, and $f_v$ is the viscous friction. The electromagnetic torque is produced by the interaction between the poles formed by the magnets on the rotor and the poles generated by the magnetomotive forces in the air gap due to the stator currents given by:

$$C_{em} = \frac{3P}{2}(\psi_r I_q + (L_d - L_q)I_d I_q), \tag{5}$$

where the coefficient $3P/2$ denote the pole-pairs. Thanks to the Phase transformation and some mathematical manipulations, the set of equations describing the NSAGPMSM are given by:

$$L_d\frac{dI_d}{d\tau} = \mu_d - RI_d + \Omega_r L_q I_q, \tag{6a}$$

$$L_q\frac{dI_q}{d\tau} = \mu_q - RI_q - \Omega_r(L_d I_d - \psi_m), \tag{6b}$$

$$J\frac{d\Omega_r}{d\tau} = \frac{3P}{2}(\psi_r I_q + (L_d - L_q)I_d I_q) - C - f_v\Omega_r. \tag{6c}$$

With the following transformations: $\mu_d = \mu_q = C = 0$, $\tau = \omega_c t$, $\omega_c = L_q/R$, $\eta_p = \frac{3P}{2}$, $\delta = \frac{L_q}{L_d}$, $\epsilon = \epsilon_0(1-\delta)$, $\epsilon_0 = \frac{\omega_c^2 k^2 L_q}{J}$, $k = \frac{f_v}{\omega_c \eta_p \psi_r}$, $\sigma = \frac{f_v \omega_c}{J}$, $\gamma = \frac{\eta_p \psi_r}{k L_q}$, $I_d = \frac{k\delta}{\eta_p} i_d$, $I_q = k i_q$, and $\Omega_r = \frac{1}{\omega_c}\omega$, the corresponding system depicting the NSAGPMSM without external disturbances are [12, 31, 32]:

$$\frac{di_d}{dt} = -\delta i_d + \eta_p j_q \omega, \tag{7a}$$

$$\frac{di_q}{dt} = -i_q - i_d\omega + \gamma\omega, \tag{7b}$$

$$\frac{d\omega}{dt} = \sigma(i_q - \omega) + \epsilon i_d i_q, \tag{7c}$$

with the currents in the q- and d-coordinates defined respectively by $i_q, i_d$, the rotor's mechanical speed given by $\omega$ and $\delta, \eta, \gamma, \sigma, \epsilon$ the constant parameters. The local maxima of $i_d$ and the corresponding greatest Lyapunov exponent (GLE) versus $\sigma$ are depicted in Fig. 2.

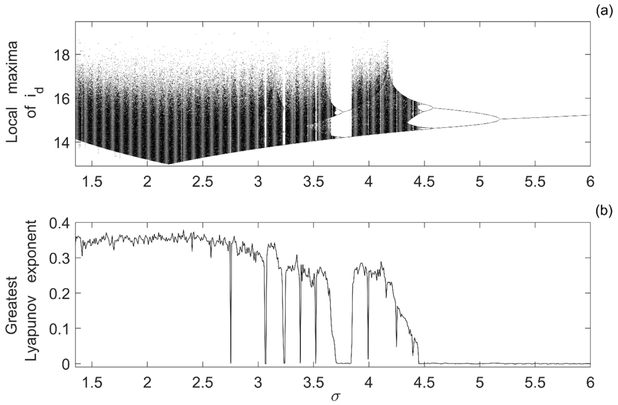

**Figure 2** (a) Local maxima of $i_d$ and associated GLE (b) versus $\sigma$ for $\epsilon = 0.41$, $\gamma = 13.27$, $\eta_p = 1.0$ and $\delta = 0.2$.

Figure 2(a) displays chaotic region with windows of periodic characteristics, reverse period doubling, and limit cycle. The GLE plot in Fig. 2(b) confirms the dynamical characteristics encountered in Fig. 2(a). The chaotic characteristics encountered in Fig. 2 are depicted in Fig. 3.

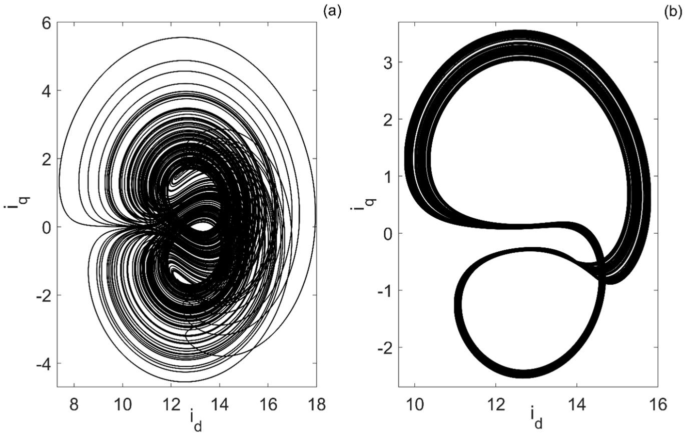

**Figure 3** Phase plane trajectories in the plane $(i_d, i_q)$ for given values of $\sigma$: (a) $\sigma = 1.4$ and (b) $\sigma = 4.44$. The other parameters are $\epsilon = 0.41$, $\gamma = 13.27$, $\eta = 1.0$, $\delta = 0.2$ and $(i_d(0), i_q(0), \omega(0)) = (0.01, 0.01, 0.01)$.

Two different shapes of chaotic characteristics are shown in Fig. 3. The shapes of chaotic attractors of Fig. 3 are different from the ones found in (Yamdjeu *et al.* 2024).

Figure 4 shows the microcontroller execution setup of NSAGPMSM described by system (7).

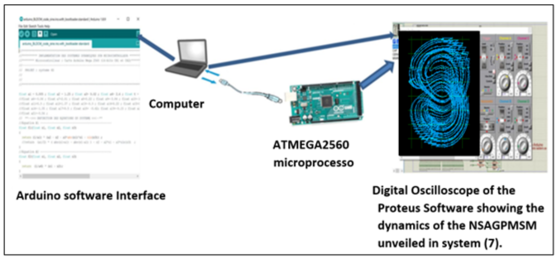

**Figure 4** Microcontroller execution setup of NSAGPMSM without external disturbances described by system (7).

Figure 4 depicts the microcontroller experimental setup comprised of the ATmega2560 microcontroller, featuring an 8-bit AVR architecture and operating at a clock speed of 16 MHz. It includes 256 KB of flash memory, with 8 KB allocated for the bootloader, along with 8 KB of static random-access memory and 4 KB of electrically erasable programmable read-only memory. The microcontroller offers 54 digital input/output pins, 16 analog input pins, and supports various communication protocols, making it ideal for complex projects. The input and output of the Arduino Mega ATMEGA2560 are respectively connected to the computer and an oscilloscope of clock frequency 16 MHz through a R-2R resistor network. The program of system (7) describing the NSAGPMSM without external disturbances solved through the $4^{\text{th}}$-order Runge-Kutta scheme using the software Arduino compiler is then inserted in the Arduino Mega microcontroller, which delivers its output signal through the R-2R resistor network. The R-2R resistor network transforms the digital signals into an equivalent analog signal, which is employed to feed the oscilloscope of the Proteus software. The dynamical characteristics encountered in Fig. 3 are established in Fig. 5 from the microcontroller execution setup of Fig. 4.

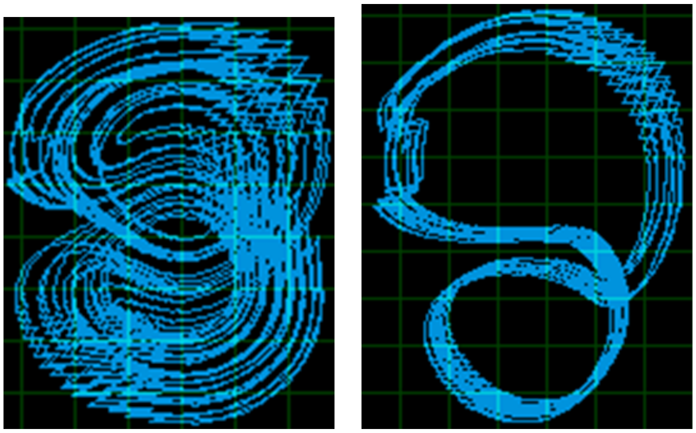

**Figure 5** Microcontroller results of NSAGPMSM without external disturbances described by system (7): (a, b) have the same parameters as those in Figs. 3 (a, b).

The experimental phase plane projections of Fig. 5 found from Fig. 4 confirm the phase plane projections of Fig. 3 obtained numerically.

## CHAOS ANNIHILATION IN NSAGPMSM WITHOUT EXTERNAL DISTURBANCES BASED ON GAS

The GAs enhances the robustness of chaotic systems by enabling global and multi-objective optimization across various engineering fields, such as mechanical, power, chemical, robotics, and aerospace engineering. They effectively control chaotic behaviors, improving safety and performance in real-world applications like ship roll and hybrid piecewise-smooth systems. Inspired by natural selection, genetic algorithms utilize concepts like fitness functions, mutation, and selection to iteratively create new populations, successfully addressing chaos in both discrete and continuous systems without needing complex derivations or integrations (Venkatesh *et al.* 2025). The chaotic characteristics encountered in NSAGPMSM without external disturbances are controlled based on GAs. The objective function is given by:

$$\text{fitness} = \frac{1}{n}\sum_{i=1}^{n} |X_i - E_i|, \tag{8}$$

where $X_i = (i_q, i_d, \omega)^t$ and $E_i$ is the equilibrium point. For $\epsilon = 0.41$, $\eta_p = 1.0$, $\sigma = 1.4$, $\delta = 0.2$, and $\gamma = 13.27$, Based on (Yamdjeu *et al.* 2024), the following three steady states are obtained for $\epsilon = 0.41$, $\eta_p = 1.0$, $\sigma = 1.4$, $\delta = 0.2$ and $\gamma = 13.27$: $E_1 = (0.0, 0.0, 0.0)^t$, $E_2 = (13.06276867, 0.7358009139, 3.550625834)^t$ and $E_3 = (13.06276867, -0.7358009139, -3.550625834)^t$. For a more stable convergence and to be adaptable to the system, the limits for each parameter $\sigma, \delta, \eta_p, \epsilon, \gamma$ are defined with the initial states $(i_q(0) = 0.01, i_d(0) = 0.01, \omega(0) = 0.01)$ after adjusting the parameters of the GAs. To suppress the chaos encountered in NSAGPMSM described by system (7) to the equilibrium point $E_1$, the optimized parameters of system (7) found are given in Table 1.

**Table 1** Optimized parameters of NSAGPMSM described by system (7) based on AGs to suppress the chaos to the equilibrium point $E_1$.

| Parameter | Value |
|---|---|
| $\sigma$ | -0.33552431 |
| $\delta$ | 3.96840578 |
| $\eta_p$ | 2.46271175 |
| $\epsilon$ | -1.77251272 |
| $\gamma$ | 8.06415182 |

Using the optimized parameters of Table 1, the objective function, change rate, error states, optimized phase diagram, and time evolutions of state variables are simulated and exposed in Fig. 6.

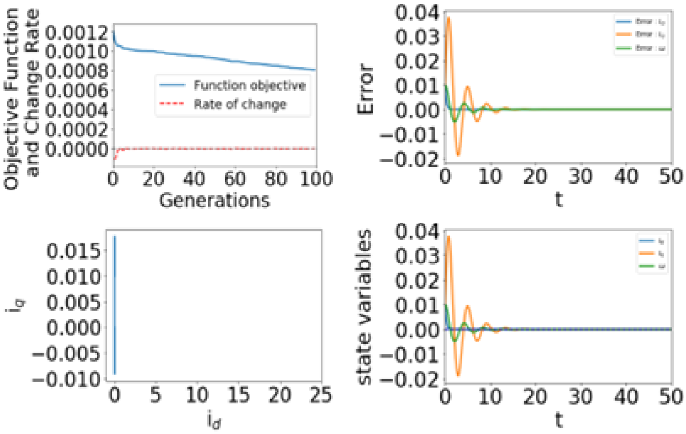

**Figure 6** (a) Objective function and convergence rate versus the iteration, (b) time evolution of the error state variables, (c) optimized phase diagram in the $(i_d, i_q)$ plane, and (d) optimized state variables.

To suppress the chaos encountered in system (7) to the equilibrium point $E_2$, the optimized parameters of system (7) found are given in Table 2.

**Table 2** Optimized parameters of NSAGPMSM described by system (7) based on AGs to suppress the chaos to the equilibrium point $E_2$.

| Parameter | Value |
|---|---|
| $\sigma$ | 0.79055438 |
| $\delta$ | 0.77378635 |
| $\eta_p$ | 3.49183549 |
| $\epsilon$ | 0.20809594 |
| $\gamma$ | 13.23148673 |

Using the optimized parameters of Table 2, the objective function, change rate, error states, optimized phase diagram, and time evolutions of state variables are simulated and exposed in Fig. 7.

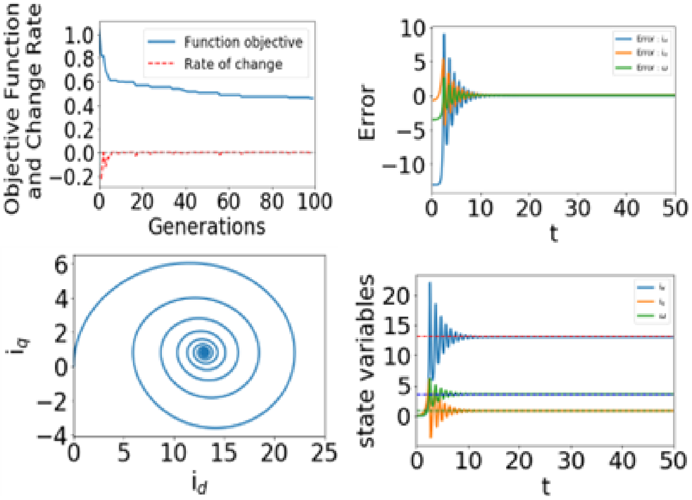

**Figure 7** (a) Objective function and convergence rate versus the iteration, (b) time evolution of the error state variables, (c) optimized phase diagram in the $(i_d, i_q)$ plane, and (d) optimized state variables.

To suppress the chaos encountered in NSAGPMSM described by system (7) to the equilibrium point $E_0$, the optimized parameters of system (7) found are given in Table 3.

**Table 3** Optimized parameters of NSAGPMSM described by system (7) based on AGs to suppress the chaos to the equilibrium point $E_0$.

| Parameter | Value |
|---|---|
| $\sigma$ | 0.921774470 |
| $\delta$ | 0.57436885 |
| $\eta_p$ | 2.85432314 |
| $\epsilon$ | 0.2727070 |
| $\gamma$ | 13.26536079 |

Using the optimized parameters of Table 3, the objective function, change rate, error states, optimized phase diagram, and time evolutions of state variables are simulated and exposed in Fig. 8.

The objective functions stabilize after decreasing with the number of iterations, and the convergence rates tend towards zero,

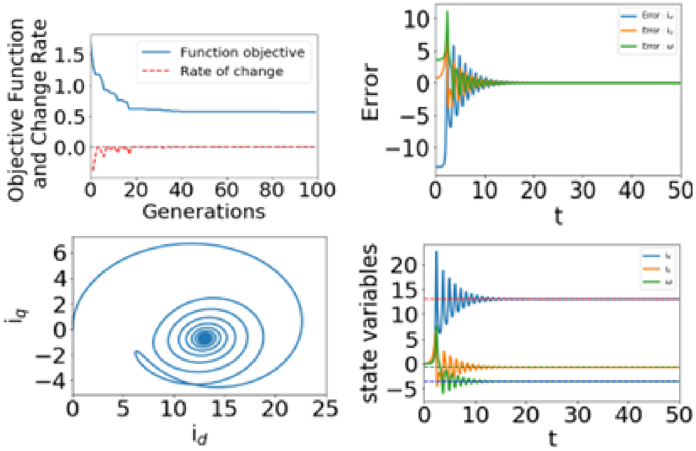

**Figure 8** (a) Objective function and convergence rate versus the iteration, (b) time evolution of the error state variables, (c) optimized phase diagram in the $(i_d, i_q)$ plane, and (d) optimized state variables.

which provides information on the efficiency and speed with which the GAs reach an optimal solution as shown in Figs. 6(a), 7(a), and 8(a). The time evolutions of the errors of the state variables in Figures 6(b), 7(b), and 8(b) converge to zero. GAs is effective to suppress chaos found in NSAGPMSM described by system (7) to the steady state $E_i$, as illustrated in Figs. 6(c, d), 7(c, d), and 8(c, d).

## CONCLUSION

The paper was devoted to the numerical, microcontroller implementation, and chaos annihilation methods in a non-smooth air-gap permanent magnet synchronous motor (NSAGPMSM) without external disturbances. Two different shapes of chaotic characteristics, reverse period doubling and periodic characteristics, were encountered in NSAGPMSM without external disturbances. These dynamical characteristics found numerically in NSAGPMSM without external disturbances were confirmed by the microcontroller execution of NSAGPMSM without external disturbances. By optimizing the parameters of NSAGPMSM without external disturbances based on genetic algorithms, the chaotic characteristics encountered in NSAGPMSM without external disturbances converged to one of its three steady states. In future considerations, additional control schemes and optimization methods such as Particle Swarm Optimization (PSO), Differential Evolution (DE), and classical Proportional-Integral-Derivative (PID) tuning will be utilized to mitigate complex behaviors in the NSAGPMSM. A comparison will be made to highlight the similarities and differences with the approaches discussed in this paper.

### Ethical standard

The authors have no relevant financial or non-financial interests to disclose.

### Availability of data and material

Not applicable.

### Conflicts of interest

The authors declare that there is no conflict of interest regarding the publication of this paper.

## LITERATURE CITED

Ananthamoorthy, N. P. and K. Baskaran, 2015 High performance hybrid fuzzy pid controller for permanent magnet synchronous motor drive with minimum rule base. Journal of Vibration and Control **21**: 181.

Caron, J. P. and J. P. Hautier, 1995 *Modélisation et commande de la machine asynchrone*, volume 10. Technip, Paris.

Chan, C. C. and K. T. Chau, 1997 An overview of power electronics in electric vehicles. IEEE Transactions on Industrial Electronics **44**: 3.

Cvetkovski, G. and L. Petkovska, 2016 Multi-objective optimal design of permanent magnet synchronous motor. In *IEEE International Power Electronics and Motion Control Conference*, p. 605.

Do, T. D., E. K. Kim, J. W. Jung, V. Q. Leu, and H. H. Choi, 2014a Adaptive pid speed control design for permanent magnet synchronous motor drives. IEEE Transactions on Power Electronics **30**: 900.

Do, T. D., E. K. Kim, J. W. Jung, V. Q. Leu, and H. H. Choi, 2014b Adaptive pid speed control design for permanent magnet synchronous motor drives. IEEE Transactions on Power Electronics **30**: 900.

Du-Qu, W. and L. Xiao-Shu, 2008 Passive adaptive control of chaos in synchronous reluctance motor. Chinese Physics **17**: 92.

Grellet, G. and G. Clerc, 1997 *Electric actuators*. Eyrolles editions.

Iqbal, A. and G. K. Singh, 2019 Chaos control of permanent magnet synchronous motor using simple controllers. Transactions of the Institute of Measurement and Control **41**: 2353.

Kemnang Tsafack, A. S., R. Kengne, J. R. M. Pone, S. Takougang Kingni, A. Cheukem, *et al.*, 2020 Spiking oscillations and multistability in nonsmooth-air-gap brushless direct current motor: Analysis, circuit validation and chaos control. International Transactions on Electrical Energy Systems **12**.

Kiener, A., P. Brissonneau, L. Brugel, and J. P. Yonnet, 1984 Conception des moteurs à aimants. Revue Générale de l'Électricité pp. 313–318.

Liao, X., F. Zhang, and C. Mu, 2017 Dynamical analysis of the permanent synchronous motor chaotic system. Advances in Difference Equations **2017**: 2.

Luo, S., 2014 Adaptive fuzzy dynamic surface control for the chaotic permanent magnet synchronous motor using nussbaum gain. Chaos **24**: 2.

Machkour, N., C. Volos, K. Kemih, H. Takhi, L. Moysis, *et al.*, 2022 Predictive control and synchronization of uncertain perturbed chaotic permanent-magnet synchronous generator and its microcontroller implementation. The European Physical Journal Special Topics **231**.

Maeng, G. and H. Choi, 2013 Adaptive sliding mode control of a chaotic nonsmooth-air-gap permanent magnet synchronous motor with uncertainties. Nonlinear Dynamics **74**: 572.

Markku, N., J. Hilla, P. Salminen, and J. Pyrhönen, 2007 Guidelines for designing concentrated winding fractional slot permanent magnet machines. In *International Conference on Power Engineering, Energy and Electrical Drives*, p. 191.

Natiq, H., J. Metsebo, A. S. Kemnang Tsafack, B. Ramakrishnan, A. C. Chamgou, *et al.*, 2022 Synchronous reluctance motor: Dynamical analysis, chaos suppression, and electronic implementation. Journal of Complexity pp. 1–7.

Pinto, T., G. Cong, T. Nguyen Vu, and Q. Vuong, 2024 Optimization design of surface-mounted permanent magnet synchronous motors using genetic algorithms. EAI Endorsed Transactions on Energy **11**: e5.

Pouillange, J. P., 1987 Les machines synchrones à aimants perma-

nents. Revue Génále de l'Électricité pp. 17–21.
Randi, S., R. Benlamine, F. Dubas, and C. Espanet, 2013 Design by optimization of an axial flux permanent-magnet synchronous motor using genetic algorithms. In *International Conference on Electrical Machines and Systems*, volume 13.
Song, J. H., Y. Cho, K. B. Lee, and Y. I. Lee, 2015 Torque-ripple minimization and fast dynamic scheme for torque predictive control of permanent magnet synchronous motors. IEEE Transactions on Industrial Electronics **30**: 2182.
Takougang Kingni, S., A. C. Chamgou, A. Cheukem, A. S. K. Tsafack, and J. R. M. Pone, 2020 Permanent magnet synchronous motor: Chaos control using single controller, synchronization and circuit implementation. SN Applied Sciences **2**.
Tian, C., C. Wu, X. Huang, and P. Zhang, 2019 Multi-physical field optimization analysis of high-speed permanent magnet synchronous motor based on nsga-ii algorithm. In *22nd International Conference on Electrical Machines and Systems*, volume 6, p. 5.
Tsapla Fotsa, R., P. K. Koubeu Papemsi, G. P. Ayemtsa Kuete, J. R. Mboupda Pone, S. R. Dzonde Naoussi, *et al.*, 2025 Title of Forthcoming Article. Chaos and Fractals **2**: 14–19, Bibliographic details are for a future publication.
Tung, P. C. and S. C. Chen, 1993 Experimental and analytical studies of the sinusoidal dither signal in a dc motor system. Dynamics and Control **3**: 54.
Venkatesh, J., A. T. Kouanou, I. K. Ngongiah, D. C. Sekhar, and S. T. Kingni, 2025 Dynamical probing and suppressing chaos using genetic algorithms in a josephson junction model with quadratic damping embedded in the microcontroller implementation. Journal of Vibration Engineering & Technologies **13**: 8–24.
Wang, J. J., D. L. Qi, and G. Z. Zhao, 2005 Multi-shelled hollow micro-/nanostructures. Journal of Zhejiang University Science **6**: 729.
Wei, Q. and X. y. Wang, 2013 Chaos controlling of permanent magnet synchronous motor base on dither signal. Journal of Vibration and Control **19**: 2541.
Yamdjeu, G., B. Sriram, S. Takougang Kingni, D. Chandra Sekhar, and A. Mohamadou, 2025 Non-smooth-air-gap permanent magnet synchronous motor under the effect of temperature embedded in the microcontroller: Dynamical appraisal and chaos suppression employing genetic algorithms. Journal of Vibration Engineering & Technologies **13**: 170.
Yamdjeu, G., B. Sriram, S. Takougang Kingni, K. Rajagopal, and A. Mohamadou, 2024 Analysis microcontroller implementation and chaos control of non-smooth air-gap permanent magnet synchronous motor. Pramana - Journal of Physics **98**: 126.
Yi, L. and A. Hsu, 2003 Efficiency optimization of brushless permanent magnet motors using penalty genetic algorithms. In *IEEE International Electric Machines and Drives Conference*, volume 1, p. 365.

***How to cite this article:*** Ngongiah, I. K., Fotsa, R. T., Ngono, J. M., Kibanya, N. N., Godwe, E., and Momo, F. Chaos Annihilation-Based on Genetic Algorithms in a Non-smooth Air-gap Permanent Magnet Synchronous Motor Embedded in the Microcontroller. *ADBA Computer Science*, 2(2), 30-35, 2025.

ADBA Computer Science
Cutting-Edge Scientific Solutions

e-ISSN: 3023-8544
RESEARCH ARTICLE
Vol.2 / No.2 / 2025 / pp.36-42
https://doi.org/10.69882/adba.cs.2025072

# Computational Study of the Effect of Aluminum Content on the Thermodynamic Properties and Phase Stability of Mg-Al-Zn Alloys

**Yusuf Uzunoğlu** *,1
*Mechanical and Metal Technologies, OSB Vocational School, Bitlis Eren University, Bitlis, Türkiye.

**ABSTRACT** This study investigates the effect of varying aluminum (Al) content on the thermodynamic properties and phase stability of Mg-Al-Zn alloys using Computational Materials Science techniques. Three Mg-Al-Zn alloys were modeled with 3 wt%, 6 wt%, and 9 wt% Al, while the zinc (Zn) content was fixed at 1 wt% and magnesium (Mg) made up the remaining balance. Phase fraction diagrams were generated using the JMatPro software to analyze the phase transformations and their evolution with temperature. Additionally, the phase compositions and thermodynamic behavior of the alloys at a fixed temperature of 300 ℃ were examined. The chemical potential ($M\mu$) of each element was calculated to assess the energy state and stability of Mg, Al, and Zn in the alloys. Furthermore, the activity values of the elements were determined to evaluate their deviations from ideal behavior and effective thermodynamic concentrations within the alloys. The results reveal that increasing Al content significantly influences the phase stability and transformation behavior of the Mg-Al-Zn system. Higher Al concentrations led to a greater proportion of the intermetallic phase ($Mg_{17}Al_{12}$) at 300 ℃, which in turn affected the chemical potential and activity of the constituent elements. This computational investigation provides insights into the role of Al in tailoring the thermodynamic properties and phase constitution of Mg-Al-Zn alloys, offering valuable guidance for alloy design and optimization in lightweight structural applications.

**KEYWORDS**
Computational materials science
Magnesium alloys
Thermodynamic properties

## INTRODUCTION

Magnesium alloys, particularly Mg-Al-Zn systems, have garnered significant attention in recent years due to their exceptional properties such as lightweight, high specific strength, and excellent corrosion resistance, making them ideal candidates for structural applications in automotive, aerospace, and electronic industries (Huang *et al.* 2023; Luo *et al.* 2012). The precise control of alloy composition, particularly the content of aluminum and zinc, plays a pivotal role in optimizing the thermodynamic and mechanical properties of these alloys. This study investigates the influence of varying aluminum concentrations (3 wt.%, 6 wt.%, and 9 wt.%) on the phase transformation behavior and thermodynamic stability of Mg-Al-Zn alloys, with zinc content fixed at 1 wt.%, through computational modeling using the JMatPro software. Previous studies have highlighted the critical role of aluminum in enhancing strength and reducing density, yet the detailed phase stability mechanisms remain underexplored (Kaya 2020; David *et al.* 2016).

The utilization of computational thermodynamics, particularly Computational Materials Science (CMS)-based software like JMatPro, has revolutionized the design and analysis of alloy systems. It provides valuable insights into phase diagrams, phase fractions, and thermodynamic properties under varying conditions (Avedesian and Baker 1999). Prior investigations have shown the effectiveness of such simulations in predicting phase equilibrium in Mg-Al-Zn alloys; however, the combined effects of aluminum variation on specific phase fractions and thermodynamic activities at intermediate temperatures, such as 300°C, remain inadequately studied (Brubaker and Liu 2004). This study aims to bridge this knowledge gap by analyzing the phase transformation diagrams, thermodynamic properties, and chemical potential of alloy components at 300°C.

In this research, the Mg-Al-Zn alloys with 3 wt.%, 6 wt.%, and 9 wt.% aluminum were simulated, and the results were compared to provide a comprehensive understanding of aluminum's impact on the alloy's phase behavior and thermodynamic stability. Additionally, the activity and chemical potential values were computed to evaluate the deviation from ideal behavior, offering insights into the energetic and interaction dynamics of the constituent elements within the alloy matrix. Previous works have shown that increased aluminum content can enhance mechanical strength but also alter the thermodynamic equilibrium (Yuzbekova *et al.* 2019; Dai *et al.* 2013). Our findings align with this observation and further elucidate the quantitative effects on phase stability and phase fraction at elevated temperatures.

---

**Manuscript received:** 28 March 2025,
**Revised:** 7 June 2025,
**Accepted:** 5 July 2025.

[1] yuzunoglu@beu.edu.tr (**Corresponding author**)

The results of this study contribute significantly to the understanding of thermodynamic behavior in Mg-Al-Zn alloys, enabling improved alloy design strategies for structural applications. By comparing the outcomes with existing literature, such as works on Mg-Zn-Al ternary phase diagrams and thermodynamic models (Hayashi *et al.* 2020; Li *et al.* 2010), this research underscores the importance of aluminum content in determining phase stability and highlights the utility of computational methods in alloy design (Uzunoğlu and Alaca 2025b; Emin *et al.* 2025). Computational methods provide significant efficiency and convenience in generating the datasets required for artificial intelligence applications in alloy design. In particular, the findings from our previous studies involving the integration of artificial intelligence with computational methods demonstrate the potential for further advancement of this approach and highlight the facilitative role of computational materials science techniques in AI-assisted alloy design (Uzunoğlu *et al.* 2025; Alaca *et al.* 2025; Uzunoğlu and Alaca 2025a).

## MATERIALS AND METHODS

In this study, the thermodynamic behavior and phase stability of Mg-Al-Zn alloys were analyzed using computational materials science techniques. The JMatPro software was employed to model and simulate three different alloy systems with varying aluminum (Al) content of 3 wt%, 6 wt%, and 9 wt%, while zinc (Zn) content was held constant at 1 wt%, and the remaining balance was magnesium (Mg). The primary objective was to investigate the influence of increasing Al content on phase transformations, chemical potential, and activity of the constituent elements within the Mg-Al-Zn system.

The methodology involved three key steps, as illustrated in the Proposed Model (Figure1):

- Alloy Modeling: The alloys were constructed by systematically varying the Al content to 3 wt%, 6 wt%, and 9 wt%, while fixing Zn at 1 wt%.

- Simulation: Phase fraction diagrams were generated for each alloy composition using JMatPro to identify the phase evolution across a temperature range. This provided insight into phase transformations as a function of Al concentration.

- Thermodynamic Calculations at 300°C: To further analyze the thermodynamic properties at a single temperature, the weight fractions of the phases, chemical potential ($M\mu$), and activity values of Mg, Al, and Zn were calculated at 300°C.

The results were evaluated to determine how increasing Al content influenced the formation and stability of phases, specifically the $Mg_{17}Al_{12}$ intermetallic phase. Additionally, the chemical potential and activity values provided a quantitative measure of the energy state and the thermodynamic behavior of each element in the alloys. This integrated approach, as summarized in Figure 1, provides a systematic framework to evaluate the effect of Al content on the thermodynamic properties of Mg-Al-Zn alloys, offering critical insights for alloy design and optimization.

### Alloy Modeling

The alloy compositions were designed by varying the aluminum content to 3 wt.%, 6 wt.%, and 9 wt.%, with the zinc content fixed at 1 wt.%, and the balance being magnesium. This compositional range was selected based on previous studies that have explored the effects of Al and Zn concentrations on the microstructure and properties of Mg-based alloys. For instance, Yu and Li investigated the precipitated phases in Al-Zn-Mg-Cu alloys, highlighting the significance of Al content in phase formation (Yu and Li 2011). Similarly, Liang et al. provided a thermodynamic description of the Al-Mg-Zn system, emphasizing the role of Al in phase stability (Liang *et al.* 1997).

### Simulation

Phase fraction diagrams for each alloy composition were generated using JMatPro, a computational tool that has been extensively utilized for modeling phase transformations in multicomponent alloys (JMatPro Sense Software Accessed in 2024). The simulations were conducted over a temperature range of 200 ° C to 600 ° C to capture the evolution of various phases, including the intermetallic phase $Mg_{17}Al_{12}$, which is known to influence the mechanical properties of Mg-Al-Zn alloys (Alidoust *et al.* 2020). The accuracy of JMatPro in predicting phase equilibria has been validated in studies such as those by Yu and Li, who modeled precipitated phases in Al-Zn-Mg-Cu alloys (Yu and Li 2011).

### Thermodynamic Calculations at 300°C

At a fixed temperature of 300 ° C, detailed thermodynamic calculations were performed to determine the weight fractions of the existing phases, as well as the chemical potential ($\mu$) and activity values of Mg, Al, and Zn. These parameters are crucial for understanding the thermodynamic stability and the deviation from ideal behavior of each element within the alloy matrix. The selection of 300 ° C is pertinent, as it aligns with temperatures commonly encountered in the processing and application of Mg-Al-Zn alloys (Zhang *et al.* 2024). The methodologies employed for these calculations are consistent with those used in prior thermodynamic analyses of similar alloy systems (Silva *et al.* 2022).

The selection of 300 ° C as evaluation temperature is highly relevant for industrial applications, particularly in the automotive and aerospace sectors, where magnesium alloys are increasingly employed for structural components that demand both lightweight and high thermal stability. Components such as engine blocks, transmission cases, and aircraft interior structures are commonly exposed to service temperatures ranging between 200°C and 350°C. At this intermediate temperature regime, the stability of intermetallic phases, such as $Mg_{17}Al_{12}$, and the thermodynamic behavior of alloying elements become critical for maintaining mechanical performance and dimensional stability. Therefore, understanding the phase constitution and chemical potential characteristics of Mg-Al-Zn alloys at 300 ° C provides practical insight into their suitability for high-temperature service conditions and helps in the development of alloys with optimized phase stability and mechanical reliability under operational stresses.

The chemical potential ($M\mu$) quantifies an element's propensity to integrate into or separate from an alloy, influenced by factors such as concentration, temperature, and pressure within the alloy matrix. A more negative chemical potential signifies a lower free energy state, indicating greater stability of the element within the alloy (Matsushita and Mukai 2018).

Activity ($\alpha$) measures the deviation of an element's behavior from ideality in an alloy. In an ideal solution, an element's activity equals its mole fraction; however, real alloys often exhibit deviations due to interactions among constituent elements (Chen 2019). Activity reflects the effective concentration of an element, contingent upon the alloy's composition, temperature, and the presence of other elements. An activity value close to 1 signifies

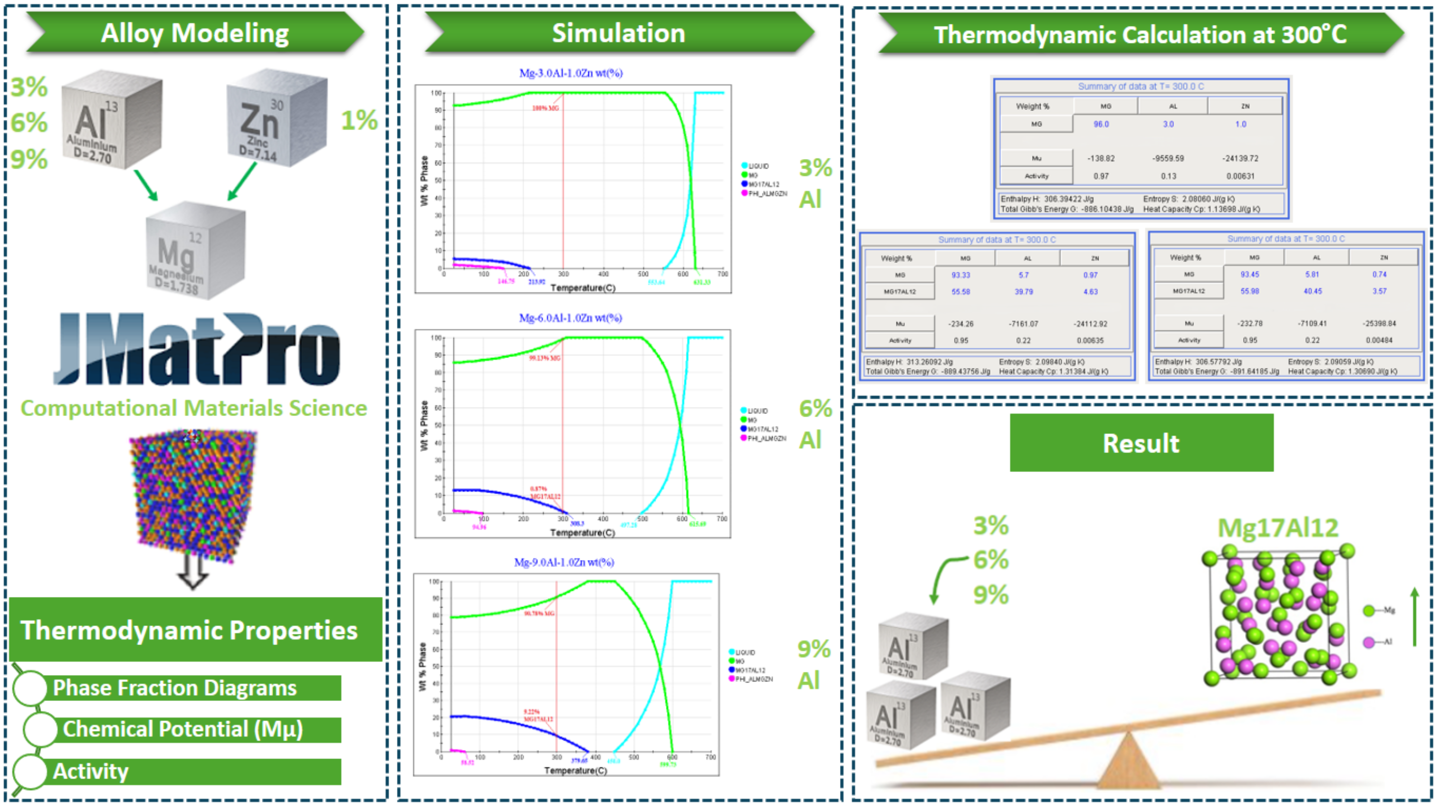

Summary of data at T= 300.0 C

| Weight % | MG | AL | ZN |
|---|---|---|---|
| MG | 96.0 | 3.0 | 1.0 |
| Mu | -138.82 | -9559.59 | -24139.72 |
| Activity | 0.97 | 0.13 | 0.00631 |

Enthalpy H: 306.39422 J/g Entropy S: 2.08060 J/(g K)
Total Gibb's Energy G: -886.10438 J/g Heat Capacity Cp: 1.13698 J/(g K)

Summary of data at T= 300.0 C

| Weight % | MG | AL | ZN |
|---|---|---|---|
| MG | 93.33 | 5.7 | 0.97 |
| MG17AL12 | 55.58 | 39.79 | 4.63 |
| Mu | -234.26 | -7161.07 | -24112.92 |
| Activity | 0.95 | 0.22 | 0.00635 |

Enthalpy H: 313.26092 J/g Entropy S: 2.09840 J/(g K)
Total Gibb's Energy G: -889.43756 J/g Heat Capacity Cp: 1.31384 J/(g K)

Summary of data at T= 300.0 C

| Weight % | MG | AL | ZN |
|---|---|---|---|
| MG | 93.45 | 5.81 | 0.74 |
| MG17AL12 | 55.98 | 40.45 | 3.57 |
| Mu | -232.78 | -7109.41 | -25398.84 |
| Activity | 0.95 | 0.22 | 0.00484 |

Enthalpy H: 306.57792 J/g Entropy S: 2.09059 J/(g K)
Total Gibb's Energy G: -891.64185 J/g Heat Capacity Cp: 1.30690 J/(g K)

**Figure 1** Proposed Model for Investigating the Thermodynamic Properties and Phase Stability of Mg-Al-Zn Alloys

ideal behavior, while values much lower than 1 indicate a significantly reduced effective concentration, meaning the element is only weakly dissolved in the alloy.

The relationship between chemical potential and activity is expressed by the equation:

$$\mu = \mu^{\circ} + RT \ln \alpha \tag{1}$$

where:

- $\mu$: Chemical potential
- $\mu^{\circ}$: Standard chemical potential of the pure element
- $R$: Universal gas constant
- $T$: Absolute temperature (Kelvin)
- $\alpha$: Activity

This equation illustrates that an increase in activity corresponds to a less negative chemical potential, signifying a higher energy state and reduced stability within the alloy (Sahoo *et al.* 2024). By integrating alloy modeling, phase diagram simulation, and thermodynamic calculations, this study provides a comprehensive understanding of how varying aluminum content affects the phase stability and thermodynamic properties of Mg-Al-Zn alloys. The findings contribute to the optimization of alloy compositions for enhanced performance in practical applications.

## RESULTS AND DISCUSSION

In this section, the results of the computational simulations and thermodynamic analyses performed on the Mg-Al-Zn alloys are presented and discussed in detail. The primary focus is on understanding the influence of increasing aluminum (Al) content (3 wt%, 6 wt%, and 9 wt%) on phase stability, chemical potential (M$\mu$), and activity of the constituent elements.

First, the phase evolution behavior of the alloys was examined through phase fraction diagrams generated using JMatPro. These diagrams illustrate the formation and stability of phases such as the primary magnesium (Mg) matrix, the intermetallic $Mg_{17}Al_{12}$ phase, and the liquid phase over a temperature range. The results highlight the relationship between Al concentration and the increasing presence of the $Mg_{17}Al_{12}$ phase, which plays a critical role in the mechanical and thermal properties of the alloys. Second, thermodynamic calculations at a fixed temperature of 300 °C provide detailed insights into the chemical potential and activity values of Mg, Al, and Zn. These parameters offer a quantitative evaluation of the energy state, stability, and effective thermodynamic concentration of each element in the alloys. Comparisons between the three alloy compositions reveal significant trends, such as the decrease in Mg chemical potential and the increase in Al contribution to phase stability with rising Al content.

The findings are analyzed in light of previous studies on Mg-Al-Zn alloys to validate the results and highlight their implications for alloy design. Trends observed in phase stability and thermodynamic behavior are discussed, with emphasis on their impact on the structural integrity and application potential of the alloys. This section provides a comprehensive evaluation of the results, correlating phase transformations with thermodynamic properties to explain the role of Al in modifying the behavior of Mg-Al-Zn systems.

### Phase Fraction Diagrams

The phase fraction diagrams for the three Mg-Al-Zn alloys, corresponding to 3 wt% Al (Figure 2), 6 wt% Al (Figure 3), and 9 wt% Al (Figure 4), were generated using JMatPro to investigate the effect of increasing Al content on the phase stability and evolution across a temperature range. These diagrams provide detailed insights into the phase transformations, including the stability of the primary magnesium (Mg) phase, the $Mg_{17}Al_{12}$ intermetallic phase, and the liquid phase.

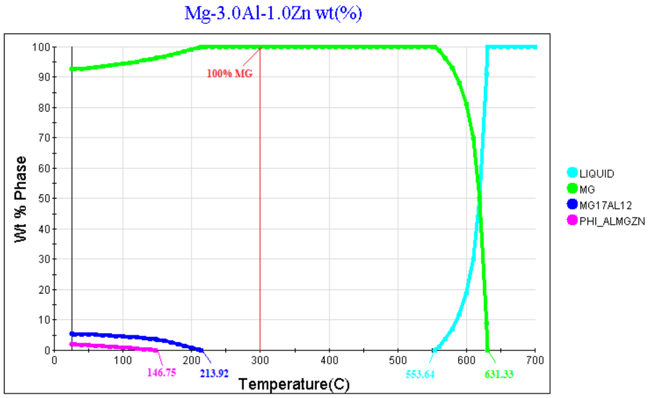

**Figure 2** Phase Fraction Diagram of Mg-3.0Al-1.0Zn Alloy. LIQUID: Represents the molten phase where the alloy constituents exist in a fully liquid state above the solidus temperature. MG: Denotes the primary magnesium-rich solid solution phase that forms the matrix of the alloy. $Mg_{17}Al_{12}$: A hard and brittle intermetallic phase known to enhance high-temperature strength but reduce ductility in magnesium alloys. PHI_AlMgZn: A ternary intermetallic phase that forms at low temperatures in the Al-Mg-Zn system, with limited thermodynamic stability and relatively low prevalence.

The phase fraction diagram for the Mg-3.0Al-1.0Zn alloy shows that the primary Mg phase (green line) dominates at low and intermediate temperatures up to approximately 553.64 °C. At this temperature, the liquid phase (cyan line) begins to form, reaching full transformation at approximately 631.33 °C. The $Mg_{17}Al_{12}$ phase (blue line) appears at lower temperatures and remains relatively low, accounting for only a small fraction (less than 5%) below 213.92 °C. This indicates that at 3 wt% Al, the alloy remains primarily composed of the Mg matrix phase, with minimal formation of the intermetallic $Mg_{17}Al_{12}$. The PHI_AlMgZn phase (magenta line) is observed only at very low temperatures (146.75 °C) and remains negligible.

The results suggest that at 3 wt% Al, the alloy exhibits high phase stability dominated by the primary Mg phase, with limited precipitation of the $Mg_{17}Al_{12}$ intermetallic. This behavior aligns with findings reported in similar Mg-Al-Zn systems, where lower Al contents result in negligible formation of secondary phases (Yu and Li 2011; Liang *et al.* 1997).

For the Mg-6.0Al-1.0Zn alloy, a notable increase in the $Mg_{17}Al_{12}$ phase fraction is observed. The primary Mg phase (green line) still dominates the microstructure but begins to decline slightly as the temperature decreases below approximately 308.3 °C. At 300 °C, the Mg phase accounts for 99.13%, with the $Mg_{17}Al_{12}$ phase (blue line) contributing 0.87%. The liquid phase (cyan line) begins to form at around 497.28 °C and becomes fully dominant by approximately 615.69 °C. The PHI_AlMgZn phase (magenta line) remains insignificant, forming only at temperatures below 100 °C and at a negligible fraction. Compared to the 3 wt% Al alloy, the increase in Al content to 6 wt% promotes the formation of the $Mg_{17}Al_{12}$ phase, albeit still at a relatively low fraction. This trend agrees with the literature, where Al is identified as a key element in the formation of intermetallic phases, which can enhance mechanical strength at elevated temperatures JMatPro Sense Software (Accessed in 2024), Alidoust *et al.* (2020). However, the dominance of the Mg phase indicates that the alloy remains largely single-phase at 300 °C.

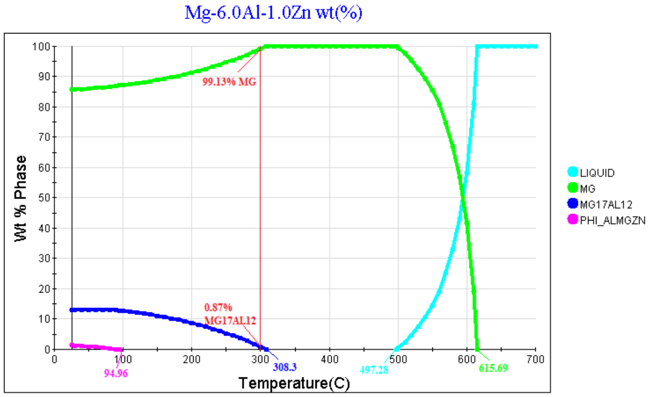

**Figure 3** Phase Fraction Diagram of Mg-6.0Al-1.0Zn Alloy

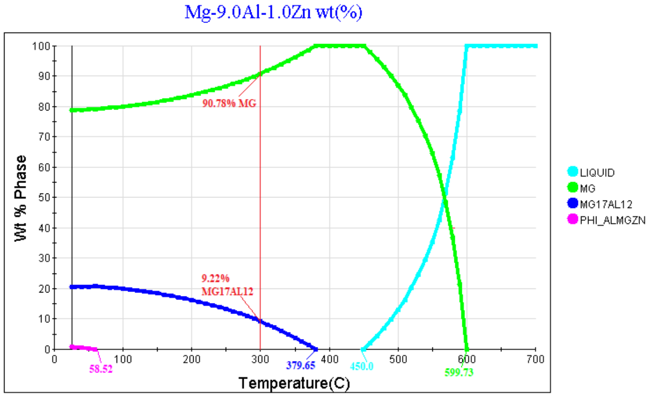

**Figure 4** Phase Fraction Diagram of Mg-9.0Al-1.0Zn Alloy

The phase fraction diagram for the Mg-9.0Al-1.0Zn alloy reveals a significant increase in the $Mg_{17}Al_{12}$ phase compared to the previous two alloys. The primary Mg phase (green line) begins to decrease more noticeably below approximately 379.65 °C, contributing 90.78% at 300 °C. Simultaneously, the $Mg_{17}Al_{12}$ phase (blue line) grows to 9.22%, indicating a substantial increase in the intermetallic fraction as Al content rises. The liquid phase (cyan line) starts to form at approximately 450.00 °C and becomes fully dominant by 599.73 °C. Similar to the previous cases, the PHI_AlMgZn phase (magenta line) remains negligible, appearing only at very low temperatures (<60 °C).

The increased formation of $Mg_{17}Al_{12}$ at 9 wt% Al highlights the critical role of aluminum in promoting this intermetallic phase. This trend is consistent with prior studies, which have shown that higher Al concentrations in Mg-Al-Zn alloys significantly enhance the stability and volume fraction of the $Mg_{17}Al_{12}$ phase (Zhang *et al.* 2024; Silva *et al.* 2022). The presence of this intermetallic phase is known to influence the alloy's mechanical properties, such as hardness and creep resistance, which are desirable for structural applications (Liang *et al.* 1997).

The phase fraction diagrams demonstrate a clear correlation between increasing Al content and the formation of the $Mg_{17}Al_{12}$ phase. At 3 wt% Al, the Mg matrix remains dominant with minimal intermetallic formation. At 6 wt% Al, a slight increase in $Mg_{17}Al_{12}$ is observed, while at 9 wt% Al, the intermetallic phase grows substantially, accounting for approximately 9.22% of the microstructure at 300 °C. These results underscore the role of aluminum as a critical element in phase evolution within Mg-Al-Zn alloys, providing valuable insights into the alloy design process for enhanced mechanical and thermodynamic properties.

### Single Calculations

To investigate the effect of aluminum (Al) content on the thermodynamic properties of Mg-Al-Zn alloys at a fixed temperature of 300 °C, single temperature calculations were performed. The weight percentages of Mg, Al, and Zn in each phase, as well as their chemical potential ($M\mu$) and activity values, were determined for the three alloy compositions: 3 wt%, 6 wt%, and 9 wt% Al. The results are presented in Figure 5, which combines the summary data for the three alloys.

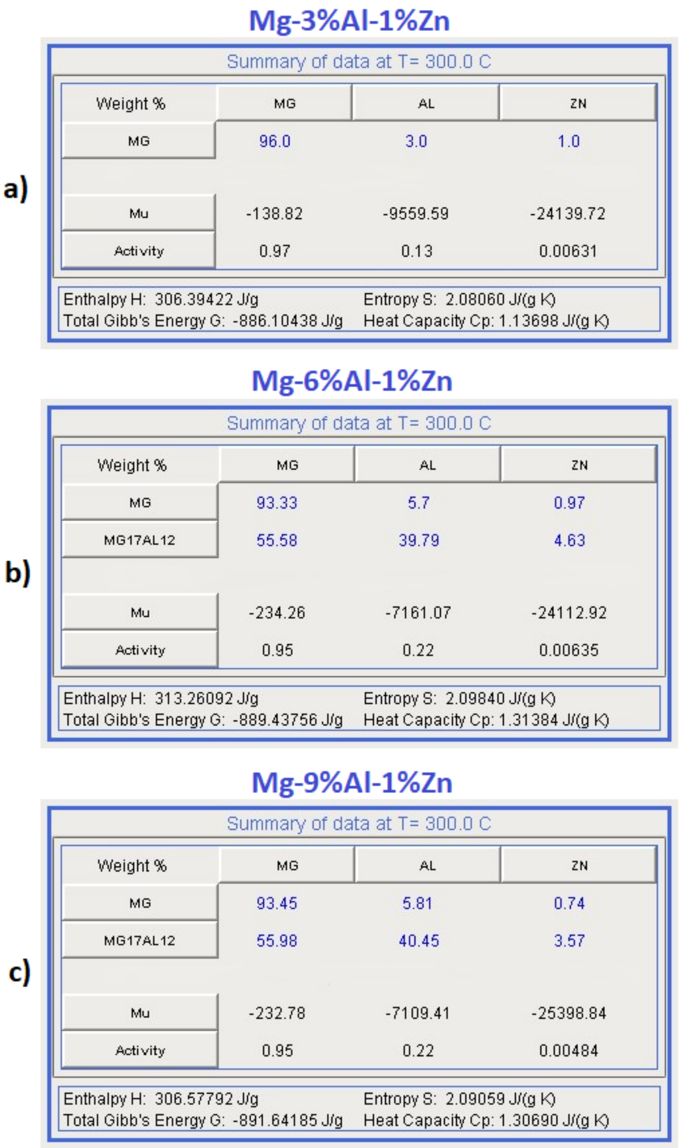

a)

Mg-3%Al-1%Zn

Summary of data at T= 300.0 C

| Weight % | MG | AL | ZN |
|---|---|---|---|
| MG | 96.0 | 3.0 | 1.0 |
| | | | |
| Mu | -138.82 | -9559.59 | -24139.72 |
| Activity | 0.97 | 0.13 | 0.00631 |

Enthalpy H: 306.39422 J/g  Entropy S: 2.08060 J/(g K)
Total Gibb's Energy G: -886.10438 J/g  Heat Capacity Cp: 1.13698 J/(g K)

b)

Mg-6%Al-1%Zn

Summary of data at T= 300.0 C

| Weight % | MG | AL | ZN |
|---|---|---|---|
| MG | 93.33 | 5.7 | 0.97 |
| MG17AL12 | 55.58 | 39.79 | 4.63 |
| | | | |
| Mu | -234.26 | -7161.07 | -24112.92 |
| Activity | 0.95 | 0.22 | 0.00635 |

Enthalpy H: 313.26092 J/g  Entropy S: 2.09840 J/(g K)
Total Gibb's Energy G: -889.43756 J/g  Heat Capacity Cp: 1.31384 J/(g K)

c)

Mg-9%Al-1%Zn

Summary of data at T= 300.0 C

| Weight % | MG | AL | ZN |
|---|---|---|---|
| MG | 93.45 | 5.81 | 0.74 |
| MG17AL12 | 55.98 | 40.45 | 3.57 |
| | | | |
| Mu | -232.78 | -7109.41 | -25398.84 |
| Activity | 0.95 | 0.22 | 0.00484 |

Enthalpy H: 306.57792 J/g  Entropy S: 2.09059 J/(g K)
Total Gibb's Energy G: -891.64185 J/g  Heat Capacity Cp: 1.30690 J/(g K)

**Figure 5** Effect of Aluminum Content on Phase Compositions, Chemical Potential, and Activity of Mg, Al, and Zn at 300 ℃

### Phase Compositions

From Figure 5, it is evident that increasing the Al content from 3 wt% to 9 wt% significantly influences the phase distribution and the composition of Mg, Al, and Zn in each phase:

Figure 5a (At 3 wt% Al): The alloy predominantly consists of the Mg phase (96.0 wt% Mg, 3.0 wt% Al, and 1.0 wt% Zn). The $Mg_{17}Al_{12}$ phase is not present at this Al concentration. Figure 5b (At 6 wt% Al): The Mg phase accounts for 93.33 wt% Mg, 5.7 wt% Al, and 0.97 wt% Zn, indicating that some Al has been partitioned into the intermetallic $Mg_{17}Al_{12}$ phase. The $Mg_{17}Al_{12}$ phase forms and contains 55.58 wt% Mg, 39.79 wt% Al, and 4.63 wt% Zn. This indicates that Al has become a significant constituent of the $Mg_{17}Al_{12}$ phase. Figure 5c (At 9 wt% Al): The Mg phase has a slightly increased Al content (5.81 wt% Al) but remains similar in Mg and Zn content (93.45 wt% Mg and 0.74 wt% Zn). The $Mg_{17}Al_{12}$ phase fraction increases, containing 55.98 wt% Mg, 40.45 wt% Al, and 3.57 wt% Zn. This trend highlights that as the Al content increases, more Al is incorporated into the $Mg_{17}Al_{12}$ phase, while Zn shows limited solubility.

### Chemical Potential ($M\mu$)

The chemical potential ($M\mu$) values of Mg, Al, and Zn provide insights into the energy states and thermodynamic stability of these elements in the alloys.

Magnesium (Mg): The chemical potential of Mg decreases slightly with increasing Al content.

**Table 1** Change in the Chemical Potential of Mg with Increasing Aluminum Content

| Aluminum Content (wt.%) | 3% Al | 6% Al | 9% Al |
|---|---|---|---|
| $M\mu_{Mg}$ (J/mol) | −138.82 | −234.26 | −232.78 |

This indicates that Mg becomes more stable (lower energy state) as Al content increases, which aligns with the formation of the intermetallic $Mg_{17}Al_{12}$ phase, consuming Al and stabilizing the Mg matrix.

Aluminum (Al): The chemical potential of Al remains significantly lower compared to Mg and Zn, reflecting its strong affinity to form intermetallic phases.

**Table 2** Change in the Chemical Potential of Al with Increasing Aluminum Content

| Aluminum Content (wt.%) | 3% Al | 6% Al | 9% Al |
|---|---|---|---|
| $M\mu_{Al}$ (J/mol) | −9559.59 | −7161.07 | −7109.41 |

As the Al content increases, the magnitude of the chemical potential becomes less negative. This suggests that excess Al is less energetically favorable in the Mg phase and preferentially partitions into the intermetallic $Mg_{17}Al_{12}$ phase.

Zinc (Zn): The chemical potential of Zn remains largely unchanged across all compositions, indicating its minimal impact on the phase transformations.

**Table 3** Change in the Chemical Potential of Zn with Increasing Aluminum Content

| Aluminum Content (wt.%) | 3% Al | 6% Al | 9% Al |
|---|---|---|---|
| $M\mu_{Zn}$ (J/mol) | −24139.72 | −24112.92 | −25398.84 |

This stability in the chemical potential of Zn suggests that Zn primarily remains in solid solution and does not significantly participate in intermetallic phase formation.

### Activity (α)

The activity values of Mg, Al, and Zn reflect their deviation from ideal behavior and effective thermodynamic concentrations within the alloy.

Magnesium (Mg): The activity of Mg decreases slightly as Al content increases.

**Table 4** Change in the Activity of Mg with Increasing Aluminum Content

| Aluminum Content (wt.%) | 3% Al | 6% Al | 9% Al |
|---|---|---|---|
| Activity of Mg ($\alpha_{Mg}$) | 0.97 | 0.95 | 0.95 |

Since all values are close to 1, it is observed that Mg behaves nearly ideally within the Mg matrix phase but shows slight deviations with increasing Al content due to the formation of the $Mg_{17}Al_{12}$ phase.

Aluminum (Al): The activity of Al increases with higher Al content but remains significantly lower than Mg.

**Table 5** Change in the Activity of Al with Increasing Aluminum Content

| Aluminum Content (wt.%) | 3% Al | 6% Al | 9% Al |
|---|---|---|---|
| Activity of Al ($\alpha_{Al}$) | 0.13 | 0.22 | 0.22 |

The low activity values (values much lower than 1) indicate that Al strongly deviates from ideal behavior due to its incorporation into the intermetallic phase, where it exhibits lower thermodynamic freedom.

Zinc (Zn): The activity of Zn remains very low across all compositions.

**Table 6** Change in the Activity of Zn with Increasing Aluminum Content

| Aluminum Content (wt.%) | 3% Al | 6% Al | 9% Al |
|---|---|---|---|
| Activity of Zn ($\alpha_{Zn}$) | 0.00631 | 0.00635 | 0.00484 |

This further supports the observation that Zn has minimal interaction with other phases and remains as a dilute solute.

In conclusion, the single temperature calculations at 300 °C demonstrate that increasing Al content leads to:

- A greater partitioning of Al into the $Mg_{17}Al_{12}$ phase, reducing its presence in the Mg phase.
- A stabilization of the Mg phase, reflected by a slight decrease in Mg's chemical potential.
- Lower chemical potential and activity values for Al, emphasizing its strong tendency to form intermetallic phases.
- Minimal changes in the chemical potential and activity of Zn, indicating its limited role in the phase transformations.

These results align with the trends observed in phase fraction diagrams and highlight the critical role of Al in determining the phase stability and thermodynamic properties of Mg-Al-Zn alloys.

## CONCLUSION

In this study, the effect of increasing aluminum (Al) content (3 wt%, 6 wt%, and 9 wt%) on the phase stability and thermodynamic properties of Mg-Al-Zn alloys was investigated using JMatPro computational materials science software. Zinc (Zn) content was held constant at 1 wt%, and the remaining balance was magnesium (Mg). Key findings from the phase fraction diagrams, single-temperature thermodynamic calculations, and chemical potential and activity analyses at 300 °C are summarized as follows:

- Phase Evolution: The phase fraction diagrams revealed that increasing Al content promotes the formation of the intermetallic $Mg_{17}Al_{12}$ phase. At 3 wt% Al, the alloy is dominated by the primary Mg phase, with negligible $Mg_{17}Al_{12}$ formation. As Al content increases to 6 wt% and 9 wt%, the volume fraction of $Mg_{17}Al_{12}$ grows significantly, highlighting the critical role of Al in phase transformation behavior.
- Thermodynamic Properties: The chemical potential ($M\mu$) of magnesium decreases slightly with increasing Al content, reflecting enhanced stabilization of the Mg phase due to Al partitioning. In contrast, the chemical potential of Al becomes less negative as it preferentially forms the $Mg_{17}Al_{12}$ phase, while the chemical potential of Zn remains relatively unchanged across all compositions.
- Activity of Elements: The activity of Mg decreases marginally with rising Al content, indicating near-ideal behavior with slight deviation due to phase interactions. Aluminum exhibits low activity, particularly at higher Al contents, emphasizing its thermodynamic preference to form intermetallic phases. Zinc maintains very low activity values, confirming its limited participation in phase transformations and its role as a dilute solute in the alloy system.
- Mechanical Properties: The formation and increased volume fraction of the $Mg_{17}Al_{12}$ intermetallic phase have notable implications for the mechanical performance of Mg-Al-Zn alloys. As a relatively hard and thermally stable phase, $Mg_{17}Al_{12}$ contributes positively to the alloy's hardness and high-temperature strength by hindering dislocation motion and improving creep resistance. However, due to its brittle nature and limited deformability, excessive formation of this

phase can detrimentally affect the alloy's ductility and impact resistance, particularly under dynamic or cyclic loading conditions. Therefore, the thermodynamically predicted increase in $Mg_{17}Al_{12}$ content with higher aluminum additions must be carefully balanced in alloy design to achieve an optimal combination of strength and toughness for structural applications. This underscores the importance of correlating phase evolution with mechanical behavior in the development of advanced Mg-based materials.

Overall, this study demonstrates that increasing Al content in Mg-Al-Zn alloys significantly influences phase stability, particularly through the formation of $Mg_{17}Al_{12}$, while stabilizing the Mg phase. These insights provide a deeper understanding of the thermodynamic behavior of Mg-Al-Zn alloys and offer a systematic framework for optimizing alloy compositions to enhance their structural performance. Future studies may explore the mechanical properties and microstructural evolution of these alloys to further validate the findings and facilitate their practical applications in lightweight structural materials.

### Ethical standard

The author has no relevant financial or non-financial interests to disclose.

### Availability of data and material

Not applicable.

### Conflicts of interest

The author declares that there is no conflict of interest regarding the publication of this paper.

## LITERATURE CITED

Alaca, Y., Y. Uzunoğlu, and B. Emin, 2025 Investigation of the effect of alloying elements on the density of titanium-based biomedical materials using explainable artificial intelligence. Computers and Electronics in Medicine **2**: 15–19.

Alidoust, M., D. Kleiven, and J. Akola, 2020 Density functional simulations of pressurized mg-zn and al-zn alloys. Physical Review Materials **4**.

Avedesian, M. and H. Baker, 1999 *Magnesium and Magnesium Alloys*. ASM International.

Brubaker, C. O. and Z.-K. Liu, 2004 A computational thermodynamic model of the ca–mg–zn system. Journal of Alloys and Compounds **370**: 114–122.

Chen, L. Q., 2019 Chemical potential and gibbs free energy. MRS Bulletin **44**: 520–523.

Dai, J. H., X. Wu, and Y. Song, 2013 Influence of alloying elements on phase stability and elastic properties of aluminum and magnesium studied by first principles. Computational Materials Science **74**: 86–91.

David, M., R. Foley, J. Griffin, *et al.*, 2016 Microstructural characterization and thermodynamic simulation of cast al–zn–mg–cu alloys. International Journal of Metalcasting **10**: 2–20.

Emin, B., Y. Uzunoğlu, and Y. Alaca, 2025 Investigation of the impact of alloying elements on the mechanical properties of superalloys using explainable artificial intelligence. Chaos and Fractals **2**: 20–27.

Hayashi, N., K. Nakashima, M. Enoki, and H. Ohtani, 2020 Thermodynamic analysis of the al-mg-zn ternary system. Journal of the Japan Institute of Metals and Materials **84**: 141–150.

Huang, X. *et al.*, 2023 Influence of aluminum content on microstructure and performance of mg-zn-ca-al-mn magnesium alloys. Journal of Alloys and Compounds **948**: 169719.

JMatPro Sense Software, Accessed in 2024 Modelling of phase transformations in magnesium alloys. https://www.sentesoftware.co.uk/site-media/mg-alloys-kinetics, [Online].

Kaya, A. A., 2020 A review on developments in magnesium alloys. Front. Mater. **7**: 198.

Li, Q., Y. Zhao, Q. Luo, S. Chen, J. Zhang, *et al.*, 2010 Experimental study and phase diagram calculation in al–zn–mg–si quaternary system. Journal of Alloys and Compounds **501**: 282–290.

Liang, H., S.-L. Chen, and Y. A. Chang, 1997 A thermodynamic description of the al-mg-zn system. Metallurgical and Materials Transactions A **28**: 1725–1734.

Luo, A. A. *et al.*, 2012 Magnesium alloy development for automotive applications. Materials Science Forum **706–709**: 69–82.

Matsushita, T. and K. Mukai, 2018 *Chemical Potential and Activity*. Springer, Singapore.

Sahoo, S. K., M. Kumar, and S. K. Karak, 2024 *Fugacity, Activity, Equilibrium Constant and Ellingham Diagram*. Springer, Singapore.

Silva, A., J. Cao, T. Polcar, and D. Kramer, 2022 Design guidelines for two-dimensional transition metal dichalcogenide alloys. Chemistry of Materials **34**: 10279–10290.

Uzunoğlu, Y. and Y. Alaca, 2025a High-accuracy prediction of the thermo-physical properties of 6xxx series aluminum alloys using explainable artificial intelligence. International Journal of Computational Materials Science and Engineering **0**: 2550010, [In Press].

Uzunoğlu, Y. and Y. Alaca, 2025b Inverse prediction of the calphad-modeled physical properties of superalloys using explainable artificial intelligence and artificial neural networks. Bitlis Eren Üniversitesi Fen Bilimleri Dergisi **14**: 331–347.

Uzunoğlu, Y., B. Emin, and Y. Alaca, 2025 High-accuracy prediction of mechanical properties of ni-cr-fe alloys using machine learning. ADBA Computer Science **2**: 7–14.

Yu, J. and X. Li, 2011 Modelling of the precipitated phases and properties of al-zn-mg-cu alloys. Journal of Phase Equilibria and Diffusion **32**: 350–360.

Yuzbekova, D., J. Borisova, and A. Mogucheva, 2019 Influence of the phase composition of al-mg alloys on the propagation of deformation bands. In *AIP Conference Proceedings*, volume 2167, p. 020395.

Zhang, Z., J. Zhang, X. Zhao, X. Cheng, X. Liu, *et al.*, 2024 Thermodynamic simulation calculations of phase transformations in low-aluminum zn-al-mg coatings. Materials **17**: 2719.

***How to cite this article:*** Uzunoğlu, Y. Computational Study of the Effect of Aluminum Content on the Thermodynamic Properties and Phase Stability of Mg-Al-Zn Alloys. *ADBA Computer Science*, 2(2), 36-42, 2025.

ADBA Computer Science
Cutting-Edge Scientific Solutions

e-ISSN: 3023-8544
RESEARCH ARTICLE
Vol.2 / No.2 / 2025 / pp.43-49
https://doi.org/10.69882/adba.cs.2025073

# A Mobile App for Enhancing Suture Skills through XAI

**Eda Nur Cumak**$^{\alpha,1}$, **Turker Berk Donmez**$^{\alpha,2}$, **Onur Kutlu**$^{\beta,3}$ **and Mustafa Kutlu**$^{\alpha,\gamma,4}$
$^{\alpha}$Department of Mechatronics Engineering, Sakarya University of Applied Sciences, Sakarya, Türkiye, $^{\beta}$Department of Surgery, University of Miami, Florida, USA, $^{\gamma}$Systems Engineering Department, Military Technological College, Muscat, Oman.

---

**ABSTRACT** This study aims to enhance the suturing skills of medical practitioners by leveraging artificial intelligence (AI) techniques. Initially, a dataset of sutures was obtained from a hospital setting and underwent preprocessing to align with the model requirements. Subsequently, data augmentation was applied to enhance the dataset for improved performance. Using transfer learning, a classification algorithm was trained on the augmented dataset with %96.59 training and %79.24 validation accuracy. To ensure interpretability, SHAP (SHapley Additive exPlanations) analysis was employed to explain the decisions made by the classification algorithm, revealing the influential pixels in suture success. In the final stage, users were introduced to the project via a mobile application developed with Flutter and Dart. This app allows users to capture images of their sutures, which are then uploaded for analysis. The SHAP analysis results are presented visually to users, indicating which parts of the suture are deemed successful and which are not via heatmaps. By providing this feedback loop, the application aims to assist medical professionals in assessing and improving their suturing skills. This study presents a valuable tool for evaluating and enhancing medical suturing abilities, with potential implications for medical education and practice. In the future this preliminary study will be test with application users which will provide continuous feedback for model refinement.

**KEYWORDS**
Suture
Transfer learning
SHAP analysis
Mobile application
Medical education

---

## INTRODUCTION

Mastering surgical skills is an essential component of medical training, crucial for aspiring clinicians as they progress towards professional competence. However, the path to acquiring these skills is filled with challenges. Traditionally, medical students have practiced suturing in hospital environments, using costly kits under the guidance of experienced professionals, either on real patients or animal models. This conventional approach, however, is marred by significant drawbacks. First of all, the financial implications of sourcing high-cost materials for suturing practice can place a considerable strain on students, particularly those navigating financial constraints.

The steep prices of suturing kits and related materials not only impose an economic burden but also threaten the inclusivity and fairness of surgical education. This may inadvertently prevent some students from acquiring critical surgical competencies (Solakoglu 2014). Furthermore, the logistical challenges of securing adequate time, space, and resources for hands-on suturing practice further complicate the learning process. The scarcity of ideal conditions for such practical training can severely limit students' opportunities to refine their suturing skills, thereby stunting their development in this essential aspect of medical practice (Haroon *et al.* 2020; Habuza *et al.* 2021). In contrast, the burgeoning field of AI is revolutionizing various facets of medicine, including educational methodologies. AI's integration into medical training, through innovative tools like surgical simulations and virtual patient scenarios, is paving the way for more effective skill acquisition. These technological advances offer a promising solution to the practical hurdles faced in traditional medical education, enabling a more efficient and engaging learning experience (Yang *et al.* 2021; Nguyen *et al.* 2021; Lekadir *et al.* 2021). Additionally, the widespread adoption of smartphones has facilitated the emergence of mobile applications equipped with AI technologies. These apps offer medical students the flexibility to practice and enhance their suturing skills anytime and anywhere, significantly expanding the avenues for practice and learning (Chakraborty *et al.* 2022; Gupta *et al.* 2022).

This study is driven by the ambition to make suturing education more accessible and impactful for medical students by leveraging the potential of AI and mobile technology. By bypassing the limitations inherent in conventional training methods, our proposed approach seeks to democratize the learning process, making it more cost-effective, flexible and conducive to skill development. Through this innovative lens, our aim is to enrich the educational landscape for medical students, ensuring they can acquire and refine their suturing skills with greater ease and efficiency (Zhang *et al.* 2023; Prentzas *et al.* 2023; Erdal *et al.* 2023).

---

**Manuscript received:** 13 June 2025,
**Revised:** 9 July 2025,
**Accepted:** 22 July 2025.

[1] edacumak@subu.edu.tr (**Corresponding author**)
[2] turkerberkdonmez@yahoo.com
[3] ock5@miami.edu
[4] mkutlu@subu.edu.tr

This study introduces a novel approach that combines Explainable AI (XAI) and mobile technology to provide an accessible, scalable, and interpretable suturing training platform. Unlike previous solutions, this study integrates SHAP analysis to enhance transparency, allowing users to understand AI decision-making processes in real-time.

The structure of this paper is organized as follows: Section offers a comprehensive background on XAI and application in health, introducing key principles and technologies that underpin our approach. In Section , the research methodology, which uses the capabilities of XAI to improve suture education, is given. Sections  and **??** present and discuss the results of XAI, respectively. Finally, Section  concludes the paper by summarizing the key findings and identifying avenues for future work, suggesting directions for further research and development in this promising field.

## RELATED WORKS

This section provides an overview of the research landscape, starting with the broad applications and challenges of XAI, with a particular emphasis on its pivotal role in healthcare and medicine. This is followed by an overview of AI-based suture training.

### XAI in Medicine

In the era marked by rapid advancements in open-source technologies, industries, including healthcare, are navigating the integration of AI into their practices. Academic research plays a pivotal role in this integration, pushing the boundaries of AI applications and fostering its adoption across various sectors, including the critical field of medicine (Haroon *et al.* 2020).

The development of AI solutions for medical decision support has been extensively reviewed by Prentzas *et al.* (2023), who emphasize the need for collaboration between medical and AI experts to design frameworks that improve the design, implementation, and evaluation of XAI. Erdal *et al.* (2023) emphasize the importance of interoperability and collaboration for adopting AI algorithms in healthcare. The healthcare sector, a primary beneficiary of these advancements, has witnessed transformative changes in service delivery, partly due to the integration of AI into medical practices. This integration has sparked interest in XAI, aiming to make AI's decision-making processes more transparent, especially in diagnostic applications (Habuza *et al.* 2021).

Significant contributions to improving the explainability of AI in medicine include studies on multimodal and multicenter data fusion techniques, as well as innovative uses of AI in combating the COVID-19 pandemic (Yang *et al.* 2021; Nguyen *et al.* 2021). AI integration into medical education has advanced significantly, especially in enhancing surgical skills. This study introduces a novel approach that combines XAI and mobile technology to provide an accessible, scalable, and interpretable suturing training platform. Unlike previous solutions, this study integrates SHAP analysis to enhance transparency, allowing users to understand AI decision-making processes in real-time ement of surgical skills. Duamwan and Bird (2023) highlight that simulation-based approaches in surgical training can be made more accessible and customized to individual needs through AI-driven models.

XAI systems, in particular, enable healthcare professionals to better understand the decision-making processes of AI algorithms, thus fostering greater trust and transparency in training. Luitse and his team illustrate that XAI, applied to cancer detection and the early diagnosis of Alzheimer's disease, visualizes the decisions made by AI models, thereby offering healthcare professionals more interpretable and reliable predictions. These techniques are also relevant to surgical training, where the interpretability of AI systems plays a significant role in advancing surgical skills.(Luitse *et al.* 2024)

The significance of AI-based imaging and analysis tools in medical education is increasingly recognized, as these tools shorten the learning curve and offer more personalized training experiences. Duamwan and Bird (2023) highlight that XAI techniques are critical not only in education but also in patient safety and treatment planning. Similarly, Luitse *et al.* (2024) demonstrate that AI approaches integrated with XAI can continuously monitor student performance in surgical training, develop individualized learning plans, and provide real-time, interpretable feedback.

### AI-Based Suture Applications

The exploration of AI's potential has led to the development of technologies aimed at improving surgical training. Earlier studies by Dubrowski *et al.* (2005); Dosis *et al.* (2005) laid the groundwork for these advancements by focusing on the quantification of forces and movements during suturing and developing a dexterity-based motion analyzer, respectively. Kil *et al.* (2017) developed a computer vision algorithm to assess suturing ability, leveraging a synthetic deep-formed platform to evaluate critical metrics related to suturing skills. Following this, Choi and Ahn (2019) introduced a flexible sensor for suture training, embedded in an artificial skin simulator to enhance the sensory training aspect of surgical skills.

Further advancements include the study by Handelman *et al.* (2020), which combined computer vision-based software with fiber optic strain sensors to evaluate suture performance in surgery. While, Mansour *et al.* (2023) has developed a computer based suture training system which employs deep learning algorithms for suture training application. This study aims to build upon these advancements by evaluating and explaining suture images with XAI. In the field of surgical simulation training, the development of AI-powered systems has rapidly advanced. However, there remains a limited number of fully automated systems utilizing Explainable AI (XAI) for the evaluation of suturing skills and surgical techniques. Existing studies primarily focus on tracking forceps movements or rely on manual video-based assessment systems (Nagaraj *et al.* 2023). AI-based solutions have made it possible to provide real-time feedback and objective evaluations during training sessions (Fukuta *et al.* 2024). Nevertheless, there is a noticeable gap in the application of XAI for the comprehensive assessment of critical skills like suturing. Thus, the incorporation of both a mobile system and XAI in our study represents a significant innovation in this area.

Previous studies in this field have predominantly focused on simulation-based systems or tracking forceps movements for surgical training and assessment, yet a fully automated system specifically for suture training has not been developed. While these works have significantly contributed to the improvement and objective evaluation of surgical skills, the absence of studies utilizing explainable artificial intelligence (XAI) in this area highlights a clear gap in the literature. Consequently, although a direct performance comparison is not feasible, our research distinguishes itself by incorporating both mobile system usage and the relatively novel approach of XAI. This combination not only enhances the usability of surgical training but also provides deeper analytical insights, setting our work apart from previous studies.

## MATERIALS AND METHODS

In this section, we outline the methodology followed in our study aimed at enhancing medical suture skills through AI and mobile technology. The approach involved several key components, including dataset acquisition, data augmentation techniques, VGG-16 transfer learning for model training, explanation of model decisions using SHAP analysis, and the development of a mobile application environment for user interaction.

### Dataset

The dataset for suture training included real images of sutures, representing different types and quality levels. Each image contained different suture examples and sutures made under various conditions. When constructing the dataset, we considered factors such as different suturing materials, thread types, and suturing techniques. This allowed our model to recognize and classify a wide range of sutures. Training subset of the dataset consists of both successful and unsuccessful suture images. This inclusion enabled our model to learn from examples of both successful and unsuccessful sutures, facilitating a more comprehensive understanding of suture quality. Furthermore, the dataset was balanced via including a sufficient number of examples representing each suture type, thereby enhancing the model's ability to accurately classify different suture characteristics. The dataset consists of 2,000 images that encompass both successful and unsuccessful suture examples, offering a robust foundation for model training and evaluation. This extensive dataset significantly enhances the model's capability to accurately differentiate between various suture characteristics. Figure 1 presents illustrative examples of both successful and unsuccessful sutures

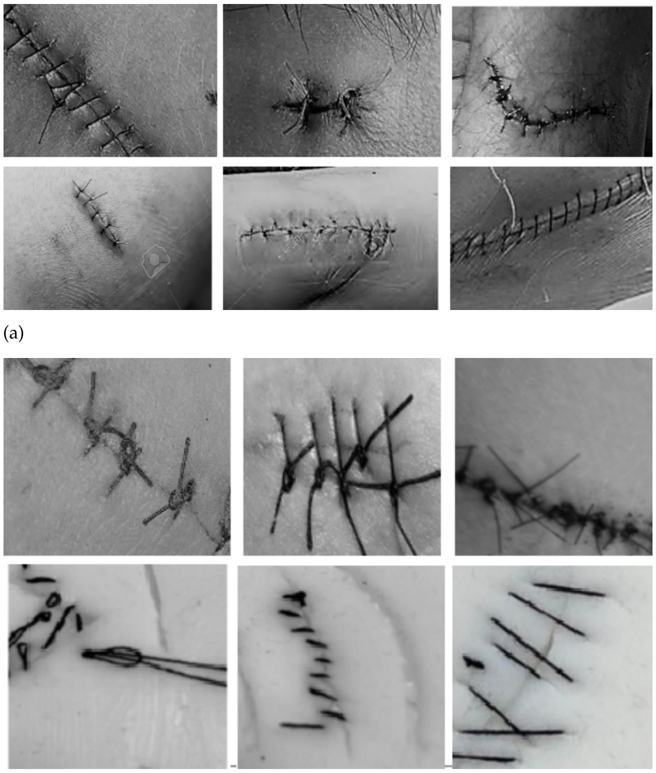
(a)

(b)

**Figure 1** Suture examples from dataset a) Successful suture examples b) Unsuccessful suture examples

### Data Augmentation

Data augmentation plays a crucial role in enhancing the robustness and generalization ability of our suture classification model. By applying various augmentation techniques to our dataset, we effectively increased its size and diversity, providing our model with a broader and more representative training example set. Techniques such as rotation, flipping, scaling, and shifting were utilized to simulate real-world variations and perspectives in suturing conditions. Additionally, random noise and distortions were introduced to images to mimic common flaws encountered in suturing tasks. This augmentation process not only expanded the dataset but also exposed the model to a wider range of suturing scenarios, thereby reducing overfitting issues. As a result, the model became more proficient in recognizing and classifying sutures under different conditions, ultimately enhancing its performance on unseen data. A series of images demonstrating these augmentation techniques is shown in Figure 2.

**Figure 2** Data augmentation techniques implemented

### Model Training

To train the suture classification model,transfer learning was employed using the VGG-16 architecture, a pre-trained convolutional neural network (CNN) widely recognized for its effectiveness in image classification tasks. Leveraging the features learned by VGG-16 on a large data set such as ImageNet, the model is adapted to our specific task of suture classification by fine-tuning its parameters on our augmented data set.

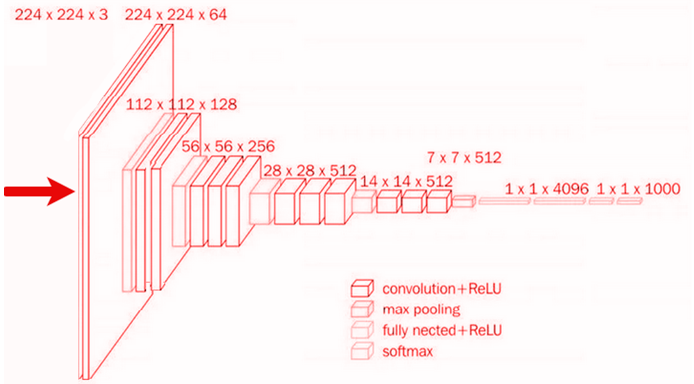

**Figure 3** VGG-16 Structure

The convolutional base layers were freezed and only training the fully connected layers, the ability to capture high-level features was retained relevant to suturing patterns while minimizing the risk of overfitting, particularly given the relatively limited size of the dataset. This approach allowed us to exploit the generalization capabilities of VGG-16 while tailoring the model to our specific domain, resulting in improved performance and speed of convergence during training.

### Model Explanation

To augment the transparency of VGG-16 model and provide clinically meaningful interpretations, SHapley Additive exPlanations (SHAP) has been employed as an interpretability tool. The Shapley value $\phi_i$ of a feature (i ) is calculated as:

$$\phi_i(f) = \sum_{S \subseteq N \setminus \{i\}} \frac{|S|! \cdot (|N| - |S| - 1)!}{|N|!} [f(S \cup \{i\}) - f(S)] \tag{1}$$

here $f(S)$ is the prediction of the model for feature subset $S$, and $N$ is the set of all features.

SHAP offers a robust and intuitive framework for explaining model predictions by quantifying the contribution of each input feature to the final output. Shapley values for each pixel were computed in the input image, which generates visualizations that highlight the significance of individual pixels in the model's decision-making process. This facilitated a deeper understanding of which regions of the image played pivotal roles in the classification process, enabling us to pinpoint areas of focus and potential biases. In Figure 4, a heatmap visualization were presented depicting the results of our SHAP analysis, providing valuable insights into the factors driving our model's predictions and enhancing transparency and interpretability.

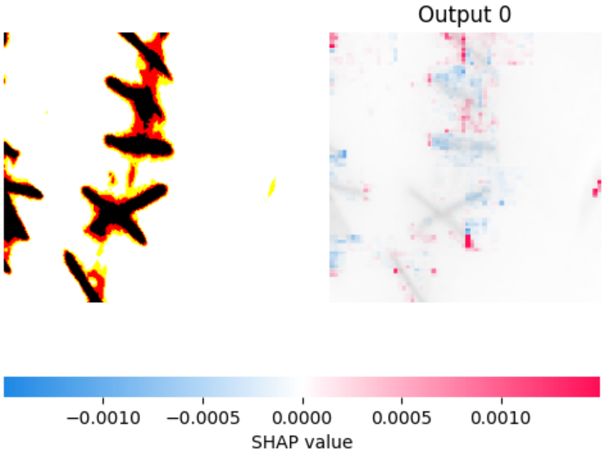

**Figure 4** Explaining the image classificiation

### Mobile App Development

In the development of our mobile application, Flutter has been employed for its efficiency and versatility in creating high-quality interfaces for both Android and iOS. The framework's rich widget library and hot reload feature greatly facilitated rapid prototyping and iterative development, allowing us to seamlessly refine user experience. Leveraging Dart, with its modern syntax, we implemented application logic and interface components that ensured a smooth and responsive user experience across various devices. Firebase played a crucial role as the app's backbone, offering a scalable and reliable infrastructure for functionalities like real-time data sync, user authentication, and cloud storage. Utilizing Firebase's Firestore database enabled efficient storage and retrieval of suture classification data, integrating seamlessly with our app and ensuring secure user authentication for personalized data access.

Our mobile application provides users the ability to capture and upload images of their suturees, receive instant feedback on classification results, and thus make informed decisions to improve their suturing skills. This capability fosters a dynamic community of enthusiasts, supported by an interface that emphasizes intuitive design, sleek navigation, and interactive features. The app's design focuses on usability and visual clarity, allowing users to easily navigate its features and access needed information.

It has been committed to continuous improvement based on user feedback, aiming to create an app that not only fulfills functional requirements but also appeals aesthetically and is user-friendly. The successful integration of Flutter and Firebase highlights the potential of these technologies to advance medical education and practice. Our application stands as a testament to the effectiveness of these tools in providing a practical, efficient, and engaging platform for medical practitioners to enhance their suturing skills.

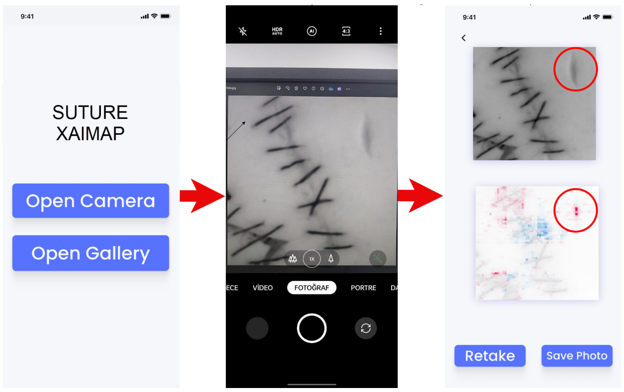

**Figure 5** UI the Mobile App

## RESULTS AND DISCUSSION

In this section, the results of training the transfer learning model for the surgical suturing task. An overview of the model's performance metrics is given in Table 1, followed by a detailed analysis of the results.

**Table 1** Hyperparameters for Transfer Learning

| Parameter | Value |
|---|---|
| Base Model | VGG-16 |
| Optimizer | Adam |
| Loss Function | Binary Crossentropy |
| Learning Rate | Default (0.001) |
| Batch Size | 32 |
| Epochs | 10 |
| **Final Training Accuracy** | 96.59% |
| **Validation Accuracy** | 79.24% |

The transfer learning model was trained using the VGG-16 architecture with hyperparameters specified in Table 1. The training process resulted in a final training accuracy of 96.59.

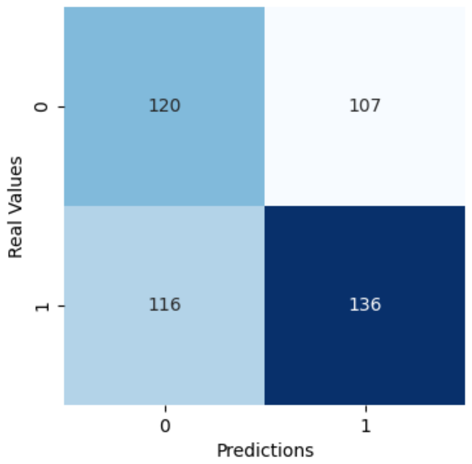

**Figure 6** Confusion matrix

In classification tasks such as surgical suture image classification, the confusion matrix plays a crucial role in evaluating the performance of the model. It provides a detailed breakdown of the model's predictions compared to the ground truth labels, allowing us to identify any patterns of misclassification. Specifically, the confusion matrix displays the true positive (TP), true negative (TN), false positive (FP), and false negative (FN) predictions. From this information, key metrics such as precision, recall, and F1-score can be calculated, providing insights into the model's ability to correctly classify different classes. Analyzing the confusion matrix allows us to identify areas where the model struggles, enabling targeted improvements to boost overall performance. Additionally, in Figure 6, the confusion matrix of the trained model is presented in its final state, providing a visual representation of the model's performance across different classes with heatmaps as shown in Figure 7.

The implications of this study are profound, extending the application of AI-driven feedback to enhance suture skills and democratize medical education (Mansour *et al.* 2023). Similarly to the advancements discussed by Kil *et al.* (2017); Choi and Ahn (2019); Handelman *et al.* (2020), this study leverages AI to make advanced training tools more accessible, echoing the need for collaboration highlighted by Prentzas *et al.* (2023); Erdal *et al.* (2023). The adoption of SHAP analysis to interpret AI decisions mirrors the movement of the broader healthcare sector toward transparent and trustworthy AI systems, underscoring the importance of explainability in AI, as advocated by Habuza *et al.* (2021) and the collaborative frameworks suggested by Prentzas *et al.* (2023). Furthermore, this study's emphasis on interdisciplinary collaboration aligns with the innovative solutions seen in the works of Dubrowski *et al.* (2005); Dosis *et al.* (2005), where technical and medical expertise converge to enhance surgical training. In the future, the integration of AI-driven feedback systems with medical training simulations could parallel the exploratory efforts in multimodal AI techniques discussed by Gupta *et al.* (2022) and the development of comprehensive tools such as those by Dosis *et al.* (2005), pushing the boundaries of surgical skill training.

This study's approach exemplifies a promising step towards leveraging AI not only to enhance specific medical skills but also to improve the accessibility and quality of medical education, resonating with the goals outlined by Chakraborty *et al.* (2022); Zhang *et al.* (2023) to use technology to advance healthcare outcomes. The find-

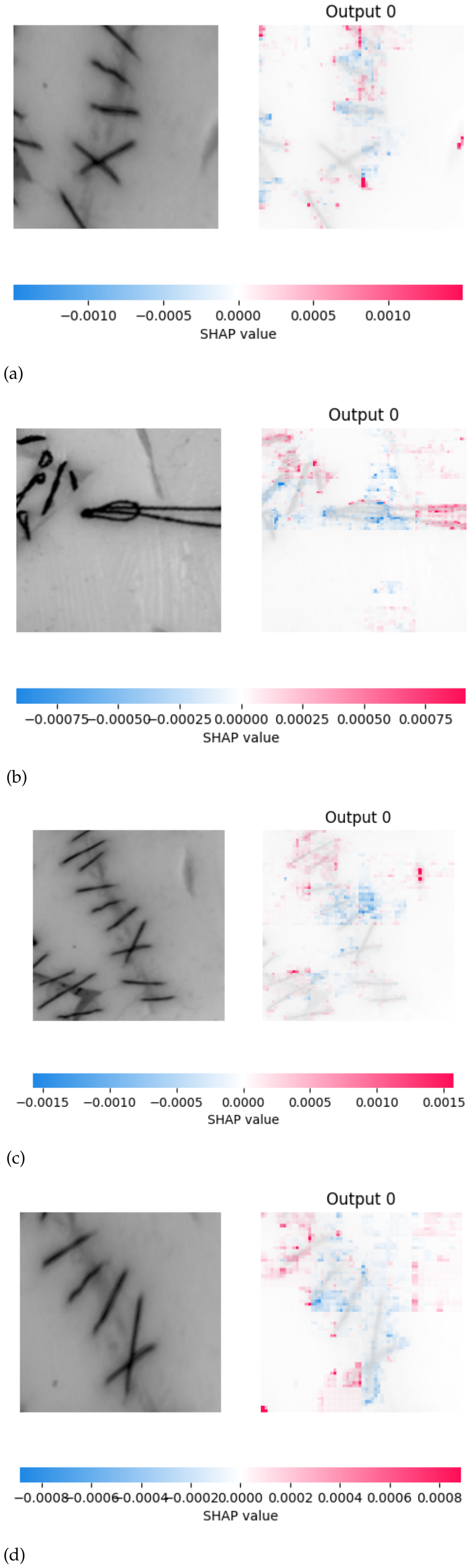

**Figure 7** Explaining examples of (a) True Positive, (b)True Negative, (c) False Positive and (d) False Negative Results

ings of this study are in line with those discussed by Dubrowski *et al.* (2005), who emphasized the importance of various criteria for skill assessment. Similarly, our study highlights the limitations of AI models in generalizing across different suture techniques. Expanding the dataset to include a wider range of procedures would improve the generalization capabilities of the model, just as strength-based metrics provide comprehensive assessment in various surgical contexts (Trejos *et al.* 2014).

The conclusions of this study align with the findings of Choi and Ahn (2019), which emphasize the importance of adapting medical training tools to varying hardware capabilities. Much like how Choi and Ahn (2019) highlighted the need for flexible solutions in diverse training environments, we recognize that the accuracy of suture classification may vary depending on mobile device specifications, such as camera quality and processing power. In response, our future work will focus on implementing advanced image processing techniques and adaptive algorithms to ensure consistent model performance across a range of devices, thus enhancing the accessibility and reliability of the application in diverse medical contexts. The development and deployment of our mobile application provide a cost-effective alternative to traditional suture training methods, which typically require professional surgeons to evaluate suture quality. Utilizing XAI on our server, the application eliminates the need for such costly assessments. This aligns with findings by Jiang *et al.* (2019), who demonstrate that mobile health apps can significantly reduce costs and enhance efficiency compared to conventional methods. Our approach thus offers a financially advantageous and effective solution for suture training.

## CONCLUSION

The results demonstrate a promising step toward the refinement of medical education, particularly in suture practice. By achieving a high training accuracy and a respectable validation accuracy, the model underscores the viability of using transfer learning to tailor preexisting, robust neural network architectures to specific medical tasks. SHAP analysis further enhances this approach by providing interpretable insights into model predictions, thereby demystifying the AI's decision-making process and fostering trust among users. The mobile application, developed using Flutter and Firebase, offers a user-friendly platform that bridges the gap between sophisticated AI models and end-users, namely medical students and professionals seeking to refine their suturing skills. The ability of the app to provide instant feedback on suturing technique represents a significant leap towards accessible, personalized medical education.

In future work, the reach and efficacy of this innovative educational tool will be improved by enriching the data set with a wider variety of suture types and conditions that could further improve the robustness and accuracy of the model. Incorporating user-generated data from the mobile app could provide a continuous feedback loop for model refinement. The next phase of this project will involve deploying the mobile application in clinical training environments to assess its impact on real-world medical education. This phase will evaluate the application's usability and its potential to enhance clinical skills training. Future iterations will include empirical testing with medical students and healthcare professionals, collecting detailed feedback on the application's effectiveness in real-world settings. Incorporating this feedback will allow us to refine the application's functionality and ensure it meets the practical needs of medical practitioners.

In the long term, AI-enhanced suture training holds the potential to improve not only medical education but also patient outcomes by providing more accessible and consistent training.

### Conflict of interest

The authors declare that they have no known competing financial interests or personal relationships that could have appeared to influence the work reported in this document.

### Data availability

The data that support the findings of this study are not openly available due to reasons of data set availability and are available from the corresponding author upon reasonable request.

### Ethical consideration

Data privacy and the potential for bias in AI models are critical ethical considerations in the deployment of AI-based medical training tools. In this study, we prioritize these concerns by ensuring that all user data is anonymized and securely stored in compliance with stringent data protection standards. Additionally, we are committed to addressing and mitigating potential biases that may arise from imbalanced datasets. This involves implementing rigorous methodologies for data collection and preprocessing to ensure fairness and representativeness. This process aims to preserve the integrity and reliability of the AI model in medical training applications.

## LITERATURE CITED

Chakraborty, S., H. Paul, S. Ghatak, S. Pandey, A. Kumar, *et al.*, 2022 An ai-based medical chatbot model for infectious disease prediction. IEEE Access .

Choi, W. and B. Ahn, 2019 A flexible sensor for suture training. IEEE Robotics and Automation Letters **4**: 4539–4546.

Dosis, A., R. Aggarwal, F. Bello, K. Moorthy, Y. Munz, *et al.*, 2005 Synchronized video and motion analysis for the assessment of procedures in the operating theater. Archives of Surgery **140**: 293–299.

Duamwan, L. M. and J. J. Bird, 2023 Explainable ai for medical image processing: a study on mri in alzheimer's disease. In *Proceedings of the 16th international conference on pervasive technologies related to assistive environments*, pp. 480–484.

Dubrowski, A., R. Sidhu, J. Park, and H. Carnahan, 2005 Quantification of motion characteristics and forces applied to tissues during suturing. The American journal of surgery **190**: 131–136.

Erdal, B. S., V. Gupta, M. Demirer, K. H. Fair, R. D. White, *et al.*, 2023 Integration and implementation strategies for ai algorithm deployment with smart routing rules and workflow management. ARXIV-CS.AI .

Fukuta, A., S. Yamashita, J. Maniwa, A. Tamaki, T. Kondo, *et al.*, 2024 Artificial intelligence facilitates the potential of simulator training: An innovative laparoscopic surgical skill validation system using artificial intelligence technology. International Journal of Computer Assisted Radiology and Surgery pp. 1–7.

Gupta, V., B. S. Erdal, C. Ramirez, R. Floca, L. Jackson, *et al.*, 2022 Current state of community-driven radiological ai deployment in medical imaging. ARXIV-CS.AI .

Habuza, T., A. N. Navaz, F. Hashim, F. Alnajjar, N. Zaki, *et al.*, 2021 Ai applications in robotics, diagnostic image analysis and precision medicine: Current limitations, future trends, guidelines on cad systems for medicine. Informatics in Medicine Unlocked .

Handelman, A., Y. Keshet, E. Livny, R. Barkan, Y. Nahum, *et al.*, 2020 Evaluation of suturing performance in general surgery and ocular microsurgery by combining computer vision-based software and distributed fiber optic strain sensors: a proof-of-concept. International Journal of Computer Assisted Radiology and Surgery **15**: 1359–1367.

Haroon, S. S., A. Viswanathan, S. Alyamkin, and R. Shenoy, 2020 Acceleration of 4ir driven digital transformation through open source: Methods and parallel industries knowledge reapplication in the field. In *Offshore Technology Conference*, p. D041S055R004, OTC.

Jiang, X., W.-K. Ming, and J. H. You, 2019 The cost-effectiveness of digital health interventions on the management of cardiovascular diseases: systematic review. Journal of Medical Internet Research **21**: e13166.

Kil, I., A. Jagannathan, R. B. Singapogu, and R. E. Groff, 2017 Development of computer vision algorithm towards assessment of suturing skill. In *2017 IEEE EMBS International Conference on Biomedical & Health Informatics (BHI)*, pp. 29–32, IEEE.

Lekadir, K., R. Osuala, C. Gallin, N. Lazrak, K. Kushibar, *et al.*, 2021 Future-ai: Guiding principles and consensus recommendations for trustworthy artificial intelligence in medical imaging. ARXIV-CS.CV .

Luitse, D., T. Blanke, and T. Poell, 2024 Ai competitions as infrastructures of power in medical imaging. Information, Communication & Society pp. 1–22.

Mansour, M., E. N. Cumak, M. Kutlu, and S. Mahmud, 2023 Deep learning based suture training system. Surgery Open Science **15**: 1–11.

Nagaraj, M. B., B. Namazi, G. Sankaranarayanan, and D. J. Scott, 2023 Developing artificial intelligence models for medical student suturing and knot-tying video-based assessment and coaching. Surgical Endoscopy **37**: 402–411.

Nguyen, D. C., M. Ding, P. N. Pathirana, and A. Seneviratne, 2021 Blockchain and ai-based solutions to combat coronavirus (covid-19)-like epidemics: A survey. ARXIV-CS.CR .

Prentzas, N., A. Kakas, and C. S. Pattichis, 2023 Explainable ai applications in the medical domain: A systematic review. ARXIV-CS.AI .

Solakoglu, Z., 2014 Evaluating the educational gains of The 6th year medical students on injection and surgical suture practices. Journal of Istanbul Faculty of Medicine **77**: 1–7.

Trejos, A. L., R. V. Patel, R. A. Malthaner, and C. M. Schlachta, 2014 Development of force-based metrics for skills assessment in minimally invasive surgery. Surgical Endoscopy **28**: 2106–2119.

Yang, G., Q. Ye, and J. Xia, 2021 Unbox the black-box for the medical explainable ai via multi-modal and multi-centre data fusion: A mini-review, two showcases and beyond. ARXIV-CS.AI .

Zhang, K., J. Yu, E. Adhikarla, R. Zhou, Z. Yan, *et al.*, 2023 Biomedgpt: A unified and generalist biomedical generative pre-trained transformer for vision, language, and multimodal tasks. ARXIV-CS.CL .

***How to cite this article:*** Cumak, E., Donmez, T. B., Kutlu, O. and Kutlu, M. A Mobile App for Enhancing Suture Skills through XAI. *ADBA Computer Science*, 2(2), 43-49, 2025.

**Computer Science**
Cutting-Edge Scientific Solutions

**e-ISSN: 3023-8544**
**RESEARCH ARTICLE**
**Vol.**2 / **No.**2 / 2025 / **pp.**50-55
https://doi.org/10.69882/adba.cs.2025074

# True Random Number Generator Design with A Fractional Order Sprott B Chaotic System

**Mehmet Ziya Hoşbaş**[*,1], **Berkay Emin**[α,2] **and Fırat Kaçar**[β,3]
[*]Department of Electronics and Automation, Technical Sciences Vocational College, Hitit University, Corum, 19100, Türkiye, [α]Osmancık Ömer Derindere MYO, Hitit University, Corum, 19500, Türkiye, [β]Department of Electrical and Electronics Engineering, Faculty of Engineering, Istanbul University-Cerrahpasa, Istanbul, 34320, Türkiye.

**ABSTRACT** The growing prevalence of digital communication and interconnected devices has amplified the need for robust data security measures. True random number generators (TRNG) play a pivotal role in protecting information by generating unpredictable and irreproducible sequences required for encryption, secure authentication, and cryptographic key generation. This research presents a TRNG model based on the fractional-order Sprott B chaotic system. The chaotic properties of the system were confirmed through Lyapunov exponent calculations, bifurcation diagrams, and phase space analyses. The fractional-order dynamics enhance the complexity and unpredictability of the generated entropy source, making it suitable for secure applications. The performance of the generated random numbers was assessed using the NIST 800-22 statistical test suite, successfully passing all tests and meeting the randomness requirements. This study introduces a unique approach by leveraging the fractional-order Sprott B chaotic system for TRNG design, demonstrating its effectiveness in cryptographic systems and secure communication frameworks.

**KEYWORDS**
Nonlinear dynamics
Chaos
TRNG
Fractional-order chaotic systems

## INTRODUCTION

True Random Number Generators (TRNGs) have become one of the foundational components of security in modern digital systems. Applications such as cryptographic key generation, authentication, digital signatures, secure communication protocols, blockchain systems, and hardware-based security modules require high-quality and unpredictable random numbers. Especially in sensitive fields such as quantum key distribution, biometric systems, and military communications, the deterministic nature of pseudo-random number generators cannot provide sufficient security, making TRNGs based on physical entropy sources the preferred choice.

For instance, in the study conducted by Park *et al.* (2020), a physically implemented TRNG design based on beta radiation was presented and optimized for low-power IoT applications. The entropy source of the TRNG relies on ionization events caused by beta particles, enabling the generation of highly secure randomness based on external physical processes. The designed TRNG was implemented at the hardware level and successfully validated through NIST 800-22 and ENT tests, demonstrating its applicability for use in IoT devices. Such studies clearly reveal that TRNGs are not only theoretically significant but also play a critical role in real-world hardware-level applications. Therefore, the development of TRNG architectures with high entropy and irreproducibility has become more important than ever for information security.

Among recent developments, FPGA-based TRNG designs have gained significant attention in recent years due to their ability to provide both high-speed performance and hardware-level flexibility. In this context, Frustaci *et al.* (2024) proposed a DSP-based true random number generator architecture optimized for FPGA implementation. The design leverages jitter from oscillator-based entropy sources and integrates a lightweight digital signal processing scheme to enhance randomness. The generated bitstreams were subjected to the NIST 800-22 statistical test suite, with results confirming that the TRNG output possesses sufficient entropy and unpredictability for cryptographic applications. This study highlights the feasibility and importance of developing efficient and secure TRNG structures directly in reconfigurable hardware environments such as FPGAs.

Similarly, Della Sala *et al.* (2022) introduced an ultra-compact TRNG architecture that is compatible with FPGA platforms and utilizes latched ring oscillators as the entropy source. The design emphasizes area-efficiency while maintaining a high level of randomness quality suitable for cryptographic uses. By exploiting the metastability behavior of digital latches in ring oscillator configurations, the proposed system ensures a non-deterministic output stream. The statistical evaluation, including NIST 800-22 tests, confirms that the TRNG meets the criteria required for secure embedded systems. This work demonstrates the potential for implementing compact and effective TRNGs within resource-constrained hardware environments.

---

**Manuscript received:** 15 January 2025,
**Revised:** 16 July 2025,
**Accepted:** 22 July 2025.

[1] mehmetziyahosbas@hitit.edu.tr(**Corresponding author**)
[2] berkayemin@hitit.edu.tr
[3] fkacar@istanbul.edu.tr

Furthermore, Garipcan and Erdem (2020) proposed a True Random Number Generator (TRNG) architecture that utilizes ring oscillators (ROs) as the physical noise source, with true randomness extracted from jitter. To enhance the statistical quality of the raw random bitstream, they introduced a novel post-processing technique based on a chaotic entropy pool, composed of discrete-time chaotic maps including quadratic, cubic, Bernoulli shift, and tent maps. Their user-controllable and dynamically adaptable post-processing structure allows the combination of multiple chaotic systems, providing both flexibility and improved entropy. The TRNG was successfully implemented on an FPGA platform, and statistical evaluations confirmed its compliance with cryptographic standards, demonstrating its effectiveness for secure hardware applications.

Among the numerous chaotic systems introduced in the literature, the Sprott B system is particularly notable due to its simple structure and rich dynamic behavior (Sprott 2003). Unlike its counterparts, the Sprott B system offers a balance between computational efficiency and chaotic complexity, making it an ideal candidate for hardware implementations of TRNGs. Despite its potential, the Sprott B system remains underexplored in the context of random number generation, particularly in fractional-order configurations.

In recent years, fractional-order chaotic systems have gained attention for their high entropy generation capabilities, making them suitable for a variety of cryptographic applications. Their inherently complex dynamic behavior and high sensitivity to initial conditions enable them to serve as effective physical entropy sources, especially in secure data transmission and image encryption. For instance, a recent study conducted a thorough numerical analysis of a fractional-order chaotic system and successfully applied its chaotic outputs in biometric data encryption (Gokyildirim *et al.* 2024). Such implementations demonstrate that chaotic systems are not only of theoretical interest but also practically viable for security mechanisms, offering alternative entropy sources for TRNG designs.

To enhance entropy diversity in chaos-based TRNG designs, exploring systems with multiple coexisting chaotic attractors offers significant advantages. Lai and Chen (2016) proposed a polynomial function-based method to extend the dynamics of the Sprott B system, enabling the generation of multiple chaotic attractors from distinct initial conditions. Their approach increases the number of index-2 saddle foci, allowing the system to exhibit two, three, or even four coexisting chaotic attractors. These attractors were validated using standard nonlinear analysis tools such as bifurcation diagrams, Lyapunov exponent spectra, and phase portraits. This method highlights the potential of structurally simple systems like Sprott B to generate rich dynamical behaviors, making them more versatile and robust candidates for secure entropy generation in hardware-based TRNGs.

(Lai *et al.* 2019), it was demonstrated that the Sprott B system can generate multiple independent chaotic and periodic attractors under different initial conditions and system parameters. Moreover, multistability was achieved in the system using a sign function, and a controller was designed to enable transitions between the chaotic attractors. This feature is particularly valuable for TRNGs designed using fractional-order chaotic systems, as it enhances the entropy generation capacity of the system and improves the quality of randomness.

Ramamoorthy *et al.* (2022) introduces a novel four-dimensional memristive extension of the Sprott B chaotic system, revealing rich dynamical behaviors including multistability, attractor coalescence, and symmetry transitions. Notably, the system is capable of transitioning between rotational symmetry and symmetry-breaking states via a tunable bias term, resulting in coexisting chaotic attractors. These phenomena, particularly partial amplitude control and offset boosting are critical for enhancing entropy generation in chaos-based TRNG designs. Such dynamic flexibility is especially relevant when employing fractional-order chaotic systems, where maximizing entropy diversity and improving randomness quality are key requirements for cryptographic robustness. The controllable multistable behavior demonstrated in this memristive system provides valuable insights for designing advanced TRNG architectures with reconfigurable entropy sources.

In this study, a novel approach for True Random Number Generator (TRNG) design is presented by integrating the fractional-order Sprott B chaotic system. The chaotic characteristics of the system are thoroughly analyzed using standard dynamical tools such as phase portraits, and its suitability for secure entropy generation has been validated (Wolf *et al.* 1985). The generated random bit sequences have been subjected to rigorous statistical evaluations, including the NIST 800-22 test suite, to confirm compliance with global randomness standards.

This research aims to fill the literature gap by demonstrating the potential of the fractional-order Sprott B system as a reliable entropy source for TRNGs. By providing both theoretical insights and practical evaluations, the study contributes to the ongoing development of secure random number generators and offers a foundation for future research in chaos-based cryptographic systems (Jun and Kocher 1999).

## FRACTIONAL ORDER SPROTT B CHAOTIC SYSTEM AND CIRCUIT REALIZATION

In 1994, Sprott (1994) introduced several chaotic systems with five and six terms, which he named A to S. These systems model chaotic behavior using simple differential equations and each of them exhibits different dynamical properties. Among them, the Sprott B chaotic system is a dynamical system described by a set of three-dimensional nonlinear differential equations and is expressed as given in Equation 1. The Sprott B system is expressed by the following autonomous differential equations:

$$\begin{aligned} \dot{x} &= yz \\ \dot{y} &= x - y \\ \dot{z} &= 1 - xy \end{aligned} \tag{1}$$

Here, $x$, $y$, and $z$ denote the state variables.

Fractional-order differential equations provide a more comprehensive mathematical framework compared to classical differential equations. This is particularly important in the analysis and control of chaotic systems, where fractional dynamics offer enhanced realism and flexibility in modeling complex behavior. In this study, the Sprott B chaotic system is formulated using fractional-order differential equations, as presented in Equation 2.

In this formulation, $x$, $y$, and $z$ are the state variables of the system, while $q_1$, $q_2$, and $q_3$ denote fractional orders of differentiation. The dynamic properties of the Sprott B system are further explored by adopting a fractional-order approach. Consequently, the system is represented as an incommensurate fractional-order chaotic model, as given in Equation 2.

$$
\begin{aligned}
D^{(q_1)}x &= yz, \\
D^{(q_2)}y &= x - y, \\
D^{(q_3)}z &= 1 - xy.
\end{aligned}
\tag{2}
$$

Here, $x$, $y$, and $z$ represent the state variables, and $D^q$ denotes the fractional-order differential operator. Parameters $a$ and $\beta$ are system-specific constants. Fractional calculus generalizes classical calculus by introducing non-integer order derivatives and integrals, denoted as $D_t^q$. This operator performs differentiation for $q > 0$ and integration for $q < 0$, and encompasses several definitions such as Grünwald–Letnikov, Riemann–Liouville, and Caputo. Among these, the Caputo definition is widely preferred due to its compatibility with classical initial conditions.

The Caputo–Euler method is a numerical technique for solving fractional differential equations based on the Caputo definition. It extends the classical Euler method by approximating fractional derivatives using a discretized form of the Caputo operator. This method iteratively computes the solution over a defined time span, making it particularly suitable for the analysis of systems exhibiting fractional-order dynamics. In this study, the Caputo–Euler method is employed to numerically solve the fractional-order differential equations. Its effectiveness in capturing complex behaviors such as chaos, phase-space evolution, and bifurcations makes it a powerful tool for investigating the dynamic properties of the system.

The practical implementation of chaotic systems on embedded platforms offers valuable opportunities for various scientific and engineering applications. In this study, the Sprott B chaotic system is implemented on the Nvidia Jetson AGX Orin embedded system platform. However, since the Nvidia Jetson AGX Orin platform does not have analog output, a 16-bit resolution TI DAC8552 based converter board with SPI interface is used to convert digital signals to analog signals [2]. The converter board is controlled by software written in Python programming language. Thanks to this approach, digital outputs are converted to analog signals with high accuracy, making it possible to make the Sprott B chaotic signal directly usable in the physical world. The general structure of the system for the application is given in Figure 1. The fractional-order Sprott B chaotic System is analyzed using the Caputo definition, with a selected order of $q = 0.9$, system parameters $a = 0.8$, $\beta = 0.82$, and initial conditions $(x_0, y_0, z_0) = (1, 1, 1)$. The aim is to investigate the influence of the fractional-order parameter $q$ on the system's dynamic and chaotic behavior. For this purpose, phase portraits and oscilloscope screenshots were generated for three different values of $q$: 0.9, 0.93, and 0.95. These visualizations serve to assess the sensitivity of the system to changes in its fractional dynamics.

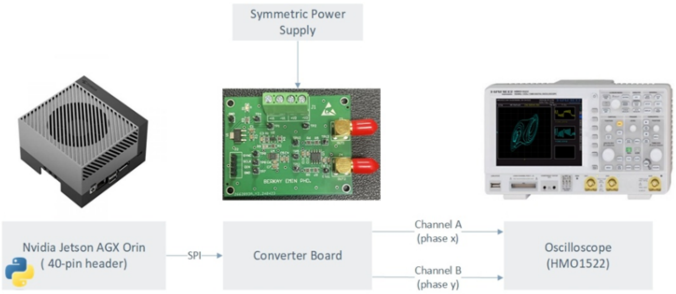

**Figure 1** General structure of the implementation system.

Figure 2 illustrates the simulation results for $q = 0.9$, revealing the system's inherent chaotic nature under the specified initial conditions and parameter set. The phase-space trajectories in the $x$-$y$, $y$-$z$, and $x$-$z$ planes, along with the corresponding oscilloscope views, depict well-developed chaotic attractors. Figure 3 presents the results for $q = 0.93$. Compared to the previous case, subtle changes in the structure and density of the trajectories are observed, indicating that small variations in $q$ significantly affect the system's dynamical characteristics. Figure 4 shows the phase portraits and oscilloscope outputs for $q = 0.95$. The attractor geometry evolves further, highlighting an increase in complexity and trajectory dispersion. This demonstrates the growing sensitivity of the system's behavior as the fractional order increases.

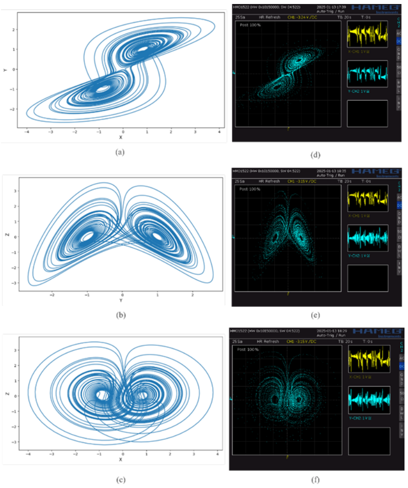

**Figure 2** Phase Portraits of Fractional Order Sprott B system for $q = 0.9$; (a) phase portrait in $x$-$y$ plane, (b) phase portrait in $y$-$z$ plane, (c) phase portrait in $x$-$z$ plane, (d) oscilloscope image of the $x$-$y$ plane, (e) oscilloscope image of the $y$-$z$ plane, (f) oscilloscope image of the $x$-$z$ plane.

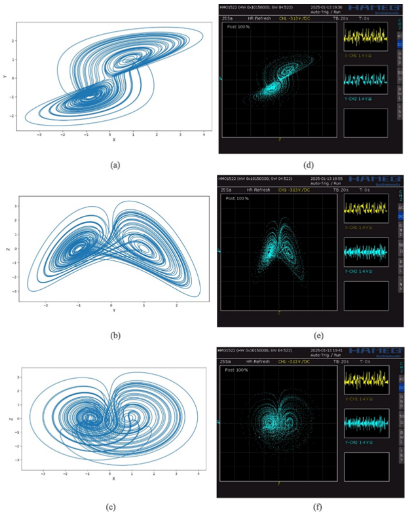

**Figure 3** Phase Portraits of Fractional Order Sprott B system for $q = 0.93$; (a) phase portrait in $x$-$y$ plane, (b) phase portrait in $y$-$z$ plane, (c) phase portrait in $x$-$z$ plane, (d) oscilloscope image of the $x$-$y$ plane, (e) oscilloscope image of the $y$-$z$ plane, (f) oscilloscope image of the $x$-$z$ plane.

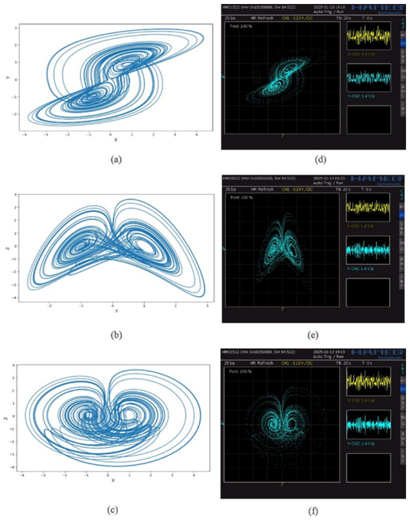

**Figure 4** Phase Portraits of Fractional Order Sprott B system for $q = 0.95$; (a) phase portrait in $x$-$y$ plane, (b) phase portrait in $y$-$z$ plane, (c) phase portrait in $x$-$z$ plane, (d) oscilloscope image of the $x$-$y$ plane, (e) oscilloscope image of the $y$-$z$ plane, (f) oscilloscope image of the $x$-$z$ plane.

## DESIGN OF A TRUE RANDOM NUMBER GENERATOR BASED ON EMBEDDED SYSTEMS

This flowchart presents the design of a True Random Number Generator (TRNG) that integrates a fractional-order Sprott B chaotic system with real-time temperature data from the Orin Nano GPU. As illustrated in Figure 5, the TRNG process follows a systematic flow to ensure high-entropy, unpredictable random bit generation.

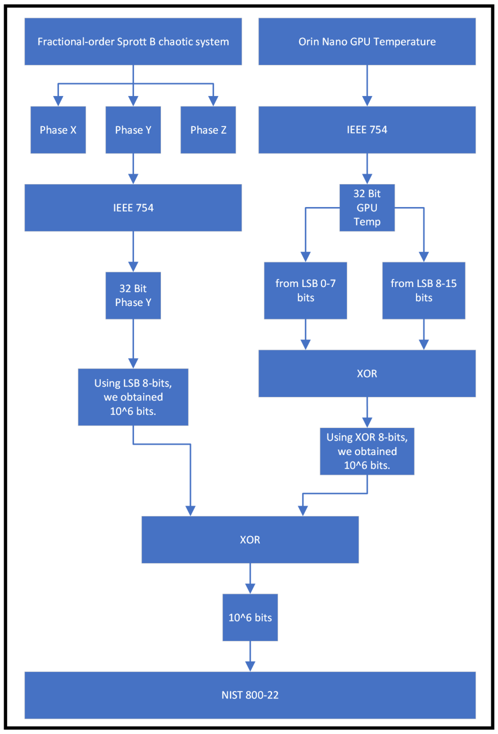

**Figure 5** Flowchart of Fractional-Order Sprott B Chaotic System-based TRNG.

The design begins with the chaotic system's outputs, which consist of three phases: Phase $X$, Phase $Y$, and Phase $Z$. These phases are converted into 32-bit floating-point representations using the IEEE 754 standard. Specifically, the Phase $Y$ output is chosen for further processing. The least significant 8 bits (LSB) from this 32-bit value are extracted to form a large dataset of random bits. This step is crucial since the LSBs in chaotic signals are typically the most unpredictable and contribute significantly to randomness. Simultaneously, the system records real-time temperature data from the Orin Nano GPU, which also undergoes conversion into a 32-bit floating-point format following the IEEE 754 standard. The system extracts two specific byte ranges from the 32-bit temperature value: the first 8 bits (LSB) and the second byte (bits 8 to 15). These two segments are combined using an XOR (exclusive OR) operation to form another sequence of random bits. This step leverages environmental variability, as temperature fluctuations introduce physical randomness.

The two independent sequences, one from the chaotic system and the other from the temperature sensorare then merged using a second XOR operation. This final XOR combination blends deterministic chaotic dynamics with physical randomness, ensuring a highly complex and unpredictable final sequence of $10^6$ bits. To validate the quality of the generated random sequence, it is subjected to the NIST 800-22 statistical test suite, a widely recognized standard for evaluating randomness. This test suite assesses various properties such as uniform distribution, independence, and unpredictability to ensure the output meets stringent international randomness standards.

In summary, the integration of the fractional-order Sprott B chaotic system and the real-time temperature data ensures that the TRNG produces a robust and secure random bit sequence. The use of chaotic phase data and temperature readings, combined through XOR operations, enhances entropy and reduces any potential correlations, making this approach suitable for cryptographic applications. The results of the NIST 800-22 statistical tests demonstrate that the random bit sequence generated by the True Random Number Generator (TRNG) meets rigorous international randomness standards. A detailed interpretation of these results is presented in Table 1.

**Table 1** NIST 800-22 Test Results for Sprott B Chaotic System-Based TRNG

| Test Type | P-Value | Conclusion |
|---|---|---|
| Frequency Test (Monobit) | 0.0672 | Passed |
| Frequency within a Block | 0.3761 | Passed |
| Run Test | 0.5410 | Passed |
| Longest Run of Ones | 0.3397 | Passed |
| Binary Matrix Rank | 0.3633 | Passed |
| DFT (Spectral) Test | 0.4408 | Passed |
| Non-Overlapping Template | 0.2993 | Passed |
| Overlapping Template | 0.0591 | Passed |
| Maurer's Universal | 0.6973 | Passed |
| Linear Complexity | 0.9899 | Passed |
| Serial Test 1 | 0.3801 | Passed |
| Serial Test 2 | 0.5467 | Passed |
| Approximate Entropy | 0.1549 | Passed |
| Cumulative Sums (Forward) | 0.0440 | Passed |
| Cumulative Sums (Reverse) | 0.1162 | Passed |
| Excursions Test $(-4)$ | 0.9233 | Passed |
| Excursions Variant $(-9)$ | 0.5929 | Passed |

The Frequency Test (Monobit) confirms that the number of 1s and 0s in the sequence is approximately equal, indicating a balanced distribution. Similarly, the Frequency Test within a Block verifies that the balance of 1s and 0s is maintained across different blocks of the sequence. The Run Test ensures that the lengths of consecutive sequences of identical bits (runs of 0s or 1s) match expected distributions for a random sequence. The Longest Run of Ones in a Block test further supports this by checking the longest sequence of 1s in each block, confirming that the bitstream does not exhibit unusual clustering.

The Binary Matrix Rank Test evaluates the rank of matrices formed from the bit sequence to detect any linear dependencies. The results show no significant linear patterns, reinforcing the randomness of the sequence. The Discrete Fourier Transform (Spectral) Test checks for periodic features and verifies the absence of predictable repeating patterns.

The Non-Overlapping Template Matching Test and Overlapping Template Matching Test search for predefined patterns in the sequence. The passing results indicate that the sequence does not show excessive occurrences of specific bit patterns, suggesting that the sequence is unpredictable. The Maurer's Universal Statistical Test assesses the compressibility of the sequence. The high $p$-value suggests that the sequence is incompressible and, therefore, random. Similarly, the Linear Complexity Test measures the complexity of the sequence by determining the shortest feedback register that could generate it. The passing result indicates that the sequence cannot be generated by a simple process.

The Serial Test checks the uniformity of overlapping bit patterns, and both sub-tests confirm that the sequence maintains a balanced distribution of these patterns. The Approximate Entropy Test further validates the sequence by ensuring that it does not contain repeating patterns beyond what would be expected in a random sequence. The Cumulative Sums (Forward and Reverse) Test examines the cumulative sum of the sequence in both forward and reverse directions, confirming that the bitstream behaves as expected for a truly random sequence.

The Random Excursions Test evaluates the number of times the cumulative sum of the sequence visits specific states within a defined range. The results show that the transitions through these states occur at frequencies consistent with random behavior. The Random Excursions Variant Test extends this analysis to a larger range of states and similarly indicates that the state transitions are consistent with randomness. In summary, the TRNG passes all tests in the NIST 800-22 suite, demonstrating that the generated sequence is uniformly distributed, free from detectable patterns, and unpredictable. These results confirm the effectiveness of the TRNG based on the fractional-order Sprott B chaotic system, making it a reliable solution for secure cryptographic applications that require high-quality random sequences.

## CONCLUSION

This study presents the design and implementation of a True Random Number Generator (TRNG) based on a fractional-order Sprott B chaotic system, demonstrating its potential as a secure entropy source for cryptographic applications. By leveraging the unique properties of fractional-order dynamics, the system enhances the unpredictability and complexity of the generated random sequences. The Caputo–Euler method was employed to solve the fractional differential equations accurately, ensuring precise modeling of the chaotic behavior. The integration of environmental entropy, in the form of real-time temperature readings from the Nvidia Jetson AGX Orin platform, further strengthens the randomness of the generated bitstreams. The combination of chaotic phase data and physical randomness using XOR operations results in a highly secure and robust random bit sequence.

The performance of the proposed TRNG was rigorously validated through the NIST 800-22 statistical test suite, where the system passed all randomness tests. This confirms that the generated sequences exhibit uniform distribution, independence, and unpredictability, satisfying stringent global randomness standards. In conclusion, the fractional-order Sprott B chaotic system provides a promising basis for TRNG design by combining mathematical richness with efficient implementation. The results indicate that this method can be effectively used in secure communication and cryptographic applications. Future work may focus on optimizing the hardware implementation and exploring the use of other fractional-order chaotic systems to further enhance entropy generation.

### Ethical standard

The authors have no relevant financial or non-financial interests to disclose.

### Availability of data and material

Not applicable.

### Conflicts of interest

The authors declare that there is no conflict of interest regarding the publication of this paper.

## LITERATURE CITED

Della Sala, R., D. Bellizia, and G. Scotti, 2022 A novel ultra-compact fpga-compatible trng architecture exploiting latched ring oscillators. IEEE Transactions on Circuits and Systems II: Express Briefs **69**: 1672–1676.

Frustaci, F., F. Spagnolo, P. Corsonello, and S. Perri, 2024 A high-speed and low-power dsp-based trng for fpga implementations. IEEE Transactions on Circuits and Systems II: Express Briefs **71**: 4964–4968.

Garipcan, A. M. and E. Erdem, 2020 A trng using chaotic entropy pool as a post-processing technique: analysis, design and fpga implementation. Analog Integrated Circuits and Signal Processing **103**: 391–410.

Gokyildirim, A., S. Çiçek, H. Calgan, and A. Akgul, 2024 Fractional-order sprott k chaotic system and its application to biometric iris image encryption. Computers in Biology and Medicine **179**: 108864.

Jun, B. and P. Kocher, 1999 The intel random number generator. Technical report, Cryptography Research, Inc.

Lai, Q. and S. Chen, 2016 Generating multiple chaotic attractors from sprott b system. International Journal of Bifurcation and Chaos **26**: 1650177.

Lai, Q., G. Xu, and H. Pei, 2019 Analysis and control of multiple attractors in sprott b system. Chaos, Solitons & Fractals **123**: 192–200.

Park, J.-M., J.-W. Lee, T.-W. Oh, Y.-H. Kim, and S.-C. Hong, 2020 A lightweight true random number generator using beta radiation for iot applications. ETRI Journal **42**: 899–909.

Ramamoorthy, R., K. Rajagopal, G. D. Leutcho, O. Krejcar, H. Namazi, *et al.*, 2022 Multistable dynamics and control of a new 4d memristive chaotic sprott b system. Chaos, Solitons & Fractals **156**: 111834.

Sprott, J. C., 1994 Some simple chaotic flows. Physical Review E **50**: 647–650.

Sprott, J. C., 2003 A simple chaotic circuit. IEEE Transactions on Circuits and Systems II: Analog and Digital Signal Processing **45**: 716–717.

Wolf, A., J. B. Swift, H. L. Swinney, and J. A. Vastano, 1985 Determining lyapunov exponents from a time series. Physica D: Nonlinear Phenomena **16**: 285–317.

***How to cite this article:*** Hoşbaş, M. Z., Emin, B., and Kaçar, F. True Random Number Generator Design with A Fractional Order Sprott B Chaotic System. *ADBA Computer Science*, 2(2), 50-55, 2025.